

Lagrangian methods for ballistic impact simulations

by

Michael Ronne Tupek

B.S., University of Wisconsin (2003)

Submitted to the Department of Mechanical Engineering
in partial fulfillment of the requirements for the degrees of
Master of Science in Mechanical Engineering
and

Master of Science in Computation for Design and Optimization
at the

MASSACHUSETTS INSTITUTE OF TECHNOLOGY

September 2010

© Massachusetts Institute of Technology 2010. All rights reserved.

MASSACHUSETTS INSTITUTE
OF TECHNOLOGY

NOV 04 2010

LIBRARIES

ARCHIVES

Author 

Department of Mechanical Engineering

August 8, 2010

Certified by

Raúl A. Radovitzky

Associate Professor of Aeronautics and Astronautics

Thesis Supervisor

Certified by

Tomasz Wierzbicki

Professor of Mechanical Engineering

Thesis Reader

Accepted by

David E. Hardt

Professor of Mechanical Engineering

Chairman, Committee for Graduate Students

Accepted by

Karen Willcox

Associate Professor of Aeronautics and Astronautics

Codirector, Computation for Design and Optimization Program

Lagrangian methods for ballistic impact simulations

by

Michael Ronne Tupek

Submitted to the Department of Mechanical Engineering
on August 8, 2010, in partial fulfillment of the
requirements for the degrees of
Master of Science in Mechanical Engineering
and
Master of Science in Computation for Design and Optimization

Abstract

This thesis explores various Lagrangian methods for simulating ballistic impact with the ultimate goal of finding a universal, robust and scalable computational framework to assist in the design of armor systems. An overview is provided of existing Lagrangian strategies including particle methods, meshless methods, and the peridynamic approach. We review the continuum formulation of mechanics and its discretization using finite elements. A rigid body contact algorithm for explicit dynamic finite elements is presented and used to model a rigid sphere impacting a confined alumina tile. The constitutive model for the alumina is provided by the Deshpande-Evans ceramic damage model. These simulations were shown to capture experimentally observed radial crack patterns. An adaptive remeshing strategy using finite elements is then explored and applied, with limited success, to the problem of predicting the transition from dwell to penetration for long-rod penetrators impacting confined ceramic targets at high velocities. Motivated by the difficulties of mesh-based Lagrangian approaches for modeling impact, an alternative Lagrangian approach is investigated which uses established constitutive relations within a particle-based computational framework. The resulting algorithm is based on a discretization of the peridynamic formulation of continuum mechanics. A validating benchmark example using a Taylor impact test is shown and compared to previous results from the literature. Further numerical examples involving ballistic impact and the crushing of an aluminum sandwich structures provide further demonstration of the method's potential for armor applications.

Thesis Supervisor: Raúl A. Radovitzky

Title: Associate Professor of Aeronautics and Astronautics

Thesis Reader: Tomasz Wierzbicki

Title: Professor of Mechanical Engineering

Contents

1	Introduction	11
1.1	Brief review of computational methods for ballistic applications . . .	12
1.1.1	Classical continuum methods: Lagrangian and Eulerian . . .	12
1.1.2	Particle and meshless methods	13
1.1.3	Peridynamics	15
1.2	Scope	16
2	Continuum formulation of mechanics and numerical discretization	17
2.1	Continuum formulation	17
2.2	Constitutive models	19
2.2.1	Ductile materials: Johnson-Cook plasticity for aluminum . . .	19
2.2.2	Brittle materials: Deshpande-Evans ceramic damage model . .	21
2.3	Continuous Galerkin finite element discretization	26
2.4	Adaptive remeshing	27
2.5	Contact algorithms	28
3	Finite element simulations of ceramic impact using damage models	33
3.1	High speed impact of ceramic tiles	34
3.1.1	Simulation setup	34
3.1.2	Simulation results	37
3.1.3	Discussion	38
3.2	Long-rod penetration of confined ceramic targets	44
3.2.1	Simulation setup	46

3.2.2	Simulation results	48
4	Peridynamics	53
4.1	Bond-based peridynamics	56
4.2	State-based peridynamics	57
4.2.1	Peridynamic states	57
4.2.2	Equations of motion	59
4.2.3	Constitutive correspondence	59
4.3	Peridynamic discretization	61
5	Peridynamic Simulations of Impact	65
5.1	Talyor impact test	66
5.2	Ballistic impact on an aluminum sandwich structure	68
5.3	Crush test of an aluminum sandwich structure	73
6	Summary and Conclusions	77
A	Deshpande-Evans Damage Model	81

List of Figures

2-1	Wing-cracks in the Deshpande-Evans ceramic model	23
3-1	Experimental setup for confined ceramic tile impact	35
3-2	Front-face and back-face ceramic impact crack patterns	36
3-3	Through slice ceramic impact crack patterns	36
3-4	Finite element mesh and simulation setup showing processor allocation	37
3-5	Ceramic tile impact simulation: coarse mesh at $t = 6\mu s$	39
3-6	Ceramic tile impact simulation: coarse mesh at $t = 12\mu s$	40
3-7	Ceramic tile impact simulation: coarse mesh at $t = 24\mu s$	41
3-8	Ceramic tile impact simulation: fine mesh at $t = 11\mu s$	41
3-9	Ceramic tile impact simulation: fine mesh at $t = 22\mu s$	42
3-10	Ceramic tile impact simulation: fine mesh at $t = 32\mu s$	42
3-11	Mesh-size dependency of damage contours on back face of ceramic tile	43
3-12	Confined SiC: transition from dwell to penetration [1]	45
3-13	Penetration depth vs. impact velocity in SiC [1]	46
3-14	Penetration velocity vs. impact velocity in SiC [1]	47
3-15	Damage contours of ceramic target impacted at 1000 m/s	49
3-16	Damage contours of ceramic target impacted at 1600 m/s: coarse mesh	51
3-17	Damage contours of ceramic target impacted at 1600 m/s: fine mesh	52
4-1	Deformation vector state (reproduced from [2])	58
5-1	Taylor impact using peridynamics	67
5-2	Schematic of sandwich panel (reproduced from [3])	69

5-3	Snapshots of sandwich panel impacted at 368 m/s	70
5-4	Snapshots of sandwich panel impacted at 531 m/s	71
5-5	Snapshots of sandwich panel impacted at 895 m/s	72
5-6	Residual velocity vs. impact velocity for sandwich panel impact [3] .	73
5-7	Crushed sandwich panels	74
5-8	Quasi-static crushed sandwich panel discretized using peridynamics .	75
5-9	Force vs. displacement curve for crushed sandwich panels	76

List of Tables

2.1	Material properties for aluminum used in the Johnson-Cook model. .	20
2.2	Material properties for alumina used in the DE ceramic model. . . .	25
5.1	Material properties for copper used in Taylor impact simulations. . .	66
5.2	Comparison of Taylor impact simulations (adapted from [4])	68

Chapter 1

Introduction

Increased interest in computational methods for simulating the response of materials and structures to impact has led to remarkable improvements in the ability to simulate complicated material behavior under dynamic conditions. The purpose of this thesis is to explore the current capabilities and their limitations in modeling ballistic impact. For concreteness and to focus on a specific problem of interest, we have restricted our attention primarily to the problem of ballistic impact on ductile and brittle targets. We focus on two specific material models, namely aluminum and alumina, which are respectively representative of the key ductile and brittle responses we aim to investigate. For the simulation of ballistic impact of these types of materials, there currently exist several computational limitations which are critical to address. In particular, there is the need to efficiently simulate detailed three dimensional aspects of the response such as the effect of structural topology and to accurately predict crack propagation and its effect on energy dissipation. Also critical is the need to overcome the limitations of the current methods in handling severe material deformations. Despite advances in the ability to describe many of the important aspects of the physics, computational approaches to the design of armor systems have yet to fully materialize. Additional important engineering applications for modeling impact other than ballistic loading of armor systems include spall impact damage in turbine engines [5], space debris impact [6], as well as geophysical problems [7].

1.1 Brief review of computational methods for ballistic applications

We proceed with a review of several of the existing computational methodologies which have been proposed to simulate impact problems. An emphasis is made on Lagrangian techniques and in particular meshless and particle based methods. Lagrangian formulations track the motion of material points moving with the body and consider the evolution of field variables such as displacements, velocities, and stresses stored at these material points. Eulerian methods consider a fixed region of space and track the flow of material through this fixed spatial domain.

1.1.1 Classical continuum methods: Lagrangian and Eulerian

Lagrangian finite element methods and Eulerian hydro-codes are both mesh-based methods and are two of the most widely used techniques for simulating impact problems and computing finite deformation material response. However, each one comes accompanied with its own set of advantages and limitations.

The advantage of Lagrangian approaches, such as finite elements, is that material histories at material points, boundaries and interfaces are all naturally tracked. The drawback is that severe deformations can result in stability problems which break the discretization. Deformations can cause the mesh to become ill-conditioned and can result in rapidly decreasing stable time steps and mesh entanglement. Additionally, the nature of the finite element discretization requires specialized techniques for modeling fracture. Common strategies for overcoming these limitations include incorporating phenomenological cohesive zone models [8] and also the practical, but less rigorous technique of element deletion or element erosion [9]. The latter, which has found widespread use in production codes, can also be used to help overcome the problem of severe mesh distortions resulting from unconstrained plastic flow. Such a technique applied at the material level is called material point deletion, and works by simply

setting the stress state to zero whenever negative Jacobians are detected. There does not exist a mathematical framework for this modification to the discretization, as it is purely an engineering solution, and it will often artificially remove mass, momentum and energy from the simulation. Approaches based on cohesive zone models have succeeded in simulating conical cracks in ceramic plates using finite elements, [10] but due to computation limitations in modeling crack surfaces the simulation were conducted in 2D, and had to include a damage model to approximate the effect of radial cracks. It has become evident that to fully capture 3D effects in ballistic impact simulations, alternative scalable algorithms must be investigated. One other approach to handle large deformations involves using finite elements, combined with the ability to adaptively remesh. This approach has shown some promise in two dimensions [10], but extensions to three dimensions have proved difficult.

Eulerian approaches have an advantage in that arbitrary material motion is permitted. These methods were originally developed for fluid dynamics applications, but have since been extended to handle materials with strength [11]. Hydro-codes such as CTH [12] can handle arbitrary material deformations, and are commonly used for ballistic impact simulations. The primary drawback of these approaches is that material point histories must be advected through the mesh, which leads to numerical diffusion and can in some instances greatly reduce numerical accuracy. Additionally, specialized algorithms for tracking interfaces and boundaries must be incorporated.

1.1.2 Particle and meshless methods

Particle based numerical methods for simulating impact problems often provide a distinct advantage in robustness over more traditional methods, such as finite elements and finite differences. The origin of such methods dates back to the smooth particle hydrodynamic (SPH) method, an idea independently introduced in the papers by Lucy [13] and Gingold and Monaghan [14]. An early review by Monaghan [15], along with a more recent review [16] discuss the many advances in techniques for overcoming some of the initial limitations of the method. The primary motivation for these particle methods comes from the astrophysics community's desire to solve

hydrodynamic PDEs, but has since been adapted by the computational solid mechanics community, where it is usually called smooth-particle applied mechanics (SPAM) [17]. Several recent papers have used the method for simulating high velocity impact [18, 19] including experimental validation using a Taylor impact test [20]. While extremely robust, the method is well known to have several computational limitations, specifically, the so-called tensile instability, zero energy modes, and difficulties with boundary conditions. Several of these issues have been resolved using somewhat ad-hoc remedies, but at the expense of additional computational costs [16, 17]. The critical advantage of the SPH and SPAM methods is their generality and robustness, in particular in the presence of severe material deformations. This has motivated the development of methods combining Lagrangian finite element methods with the ability to convert elements into SPH particles dynamically during a simulation when elements become too distorted [21].

Meshless methods are another family of methods which have shown promise for ballistic impact problems involving large deformations. Meshless methods based on the Galerkin procedure for solving partial differential equations were first proposed in a paper by Nayroles on the diffuse element method [22] and further developed by Belytschko with the element-free Galerkin (EFG) method [23]. Various other extensions, improvements, generalizations and alternative formulations have been explored since, including the reproducing kernel particle method (RKPM) [24],[25], h-p clouds [26], partition of unity [27], the local meshless Petrov-Galerkin method (MLPG) [28], the method of finite spheres [29] and the local maximum entropy method [30]. The MLPG method has been validated using a Taylor impact benchmark test [31] and has been shown to be more robust for problems involving ballistic impact than a finite element approach. An extension of the EFG method using moving least square (MLS) approximations combined with an extrinsic crack field enrichment has been successfully applied in two dimensions to a high-speed ballistic impact [32]. An interesting recent development in meshless methods uses ideas from variational calculus and in particular, optimal transportation theory, combined with maximum entropy meshfree interpolations [30, 4]. The method has been successfully applied to prob-

lems in both fluid and computational mechanics and has been validated using the Taylor impact benchmark problem [4]. Most of these methods overcome some of the specific shortcomings of SPH methods, however the associated computational costs are relatively high, which could hinder their widespread use.

An alternative hybrid particle/mesh-based method, originating with the Hamiltonian particle hydrodynamics method, avoids the tensile and boundary instabilities known to plague many particle based methods [33]. The algorithm works by using particles to model contact and impact, as well as material response under compression, while a finite element discretization is used to compute tensile and shear response. The method has been applied to various problems, including hypervelocity impact [33] and orbital debris impact [6]. The method is further improved by a parallel implementation which helps its efficiency. While the method should excel for modeling brittle materials, it is still limited for ductile materials undergoing large shear strains, as elements are still prone to failure in tension and shear.

1.1.3 Peridynamics

In this thesis we have given particular attention to a recently proposed particle based method, which we believe has the potential to address several of the limitations of existing methods. This class of numerical methods is based on a reformulated theory of continuum mechanics, coined by its author as peridynamics [34, 2]. The peridynamic theory allows for non-local material point interactions, and thus introduces a characteristic physical length scale, which is necessary for modeling damage. The numerical discretization of this formulation results in a particle based algorithm which stores both field and material state variables at the same discretization locations. Although many theoretical aspects remain to be investigated, it is possible that the theory will provide a rigorous unifying mathematical framework for general classes of particle based and meshless methods. This framework may additionally help to understand limitations in existing methods.

1.2 Scope

In this thesis, we experiment with different computational methodologies with a view towards a universal, robust, and scalable simulation framework for impact problems. In Chapter 2, we review the theoretical and computational framework of continuum mechanics and finite elements. We describe the specific constitutive models used for aluminum and alumina. These are a modified Johnson-Cook isotropic metal plasticity model with damage [35, 36] and the Deshpande-Evans ceramic model with damage [37]. A novel rigid body contact algorithm is described, inspired by Cirak and West’s decomposition contact response algorithm. Artificial viscosity and adaptive remeshing algorithms were used to overcome some of the computational challenges caused by the severe deformations which occur due to ballistic impact. In Chapter 3, we provide examples illustrating the capabilities of this computational framework applied to problems involving ballistic impact on ceramic targets. The examples demonstrate the ability and limitations of the finite element approach in predicting radial crack patterns and the transition from dwell to penetration for a projectile impacting confined ceramic targets. Chapter 4 introduces the new continuum theory of peridynamics proposed by Silling [2] and its numerical discretization as a particle based method. We believe that this new formulation will enable a more efficient and robust computational framework to predict the physical response of materials subjected to impact. In Chapter 5, numerical examples are provided which validate the peridynamic discretization, including a sample impact problem with failure. Chapter 6 summarizes and concludes with the successes and failures of the different approaches, and provides an outlook for future developments.

Chapter 2

Continuum formulation of mechanics and its numerical discretization

The impact of solid materials is described by the equations of continuum mechanics. Most of the physical phenomena observed experimentally in impact events can be described withing this framework, specifically elastic deformations, lattice plasticity, damage and fracture. For completeness, we summarize the relevant physical equations which model the mechanics of continua.

2.1 Continuum formulation

We begin by considering the motion of a arbitrary body. At a material point, \mathbf{X} , in the reference configuration of a body occupying a region $B_0 \subset \mathbb{R}^3$ at time $t = t_0$, the current configuration of the body at some time t in the interval $T = [t_0, t_f]$ is described through the deformation mapping

$$\mathbf{x} = \boldsymbol{\varphi}(\mathbf{X}, t) \quad \forall \mathbf{X} \in B_0, \quad \forall t \in T \quad (2.1)$$

The deformation within an infinitesimal material region is assumed to be fully described by the deformation gradient

$$\mathbf{F} = \nabla_0 \boldsymbol{\varphi}(\mathbf{X}, t) \quad \forall \mathbf{X} \in B_0, \quad \forall t \in T, \quad (2.2)$$

where ∇_0 is the material gradient defined on B_0 . The determinant of \mathbf{F} is the Jacobian, and is a measure of the ratio of the deformed to undeformed volume and must be positive,

$$J = \det(\mathbf{F}) > 0 \quad \forall \mathbf{X} \in B_0, \quad \forall t \in T. \quad (2.3)$$

Balance of linear momentum over the body requires

$$\nabla_0 \cdot \mathbf{P} + \rho_0 \mathbf{B} = \rho_0 \ddot{\boldsymbol{\varphi}} \quad \forall \mathbf{X} \in B_0, \quad \forall t \in T \quad (2.4)$$

$$\mathbf{P} \cdot \mathbf{N} = \mathbf{T} \quad \forall \mathbf{X} \in \partial B_0, \quad \forall t \in T \quad (2.5)$$

where \mathbf{B} is the body force, \mathbf{T} is the externally applied tractions, $\mathbf{P} = \frac{\partial W}{\partial \mathbf{F}}(\mathbf{F})$ is the first Piola-Kirchhoff stress tensor, and \mathbf{N} is the outward reference unit surface normal. Conservation of angular momentum requires the Cauchy stress $\boldsymbol{\sigma} = \mathbf{P}\mathbf{F}^T/J$ to be symmetric.

We decompose the Piola-Kirchhoff stress tensor \mathbf{P} into an equilibrium part \mathbf{P}^e and a viscous part \mathbf{P}^v :

$$\mathbf{P} = \mathbf{P}^e + \mathbf{P}^v \quad (2.6)$$

If we assume Newtonian viscosity, then the viscous Cauchy stress $\boldsymbol{\sigma}^v$ is given by

$$\boldsymbol{\sigma}^v = 2\eta_h(\text{sym}\dot{\mathbf{F}}\mathbf{F}^{-1})^{\text{dev}} \quad (2.7)$$

where η_h is the Newtonian viscosity coefficient, and sym and dev denote the symmetric and deviatoric components of a tensor. \mathbf{P}^v can then be obtained as

$$\mathbf{P}^v(\dot{\mathbf{F}}, \mathbf{F}) = J\boldsymbol{\sigma}^v\mathbf{F}^{-T}. \quad (2.8)$$

We will often add some artificial viscosity into the constitutive response to alleviate numerical issues that arise in problems involving shocks [38].

2.2 Constitutive models

To complete the continuum description for materials with strength, we specify a constitutive relation which relates the deformation kinematics with the Piola-Kirchhoff stress at each material point. Throughout this work, we primarily limit ourselves to two specific constitutive relations for modeling aluminum and alumina, which are respectively representative ductile and brittle materials used in armor technology. Material damage for both ductile and brittle materials is described via the commonly adopted approach of continuum damage models. These models are used to predict the onset of fracture and often assume that the material softens as damage accumulates. The convergence limitations for this class of models is well known [39], but despite this, they are still used successfully in many engineering situations.

2.2.1 Ductile materials: Johnson-Cook plasticity with damage for 6061-T6 aluminum

A large number of models and computational algorithms have emerged for describing inelastic material response [40, 41]. These models have been developed to predict material response under a variety of different operating conditions, strain rates and temperatures. For this thesis, the experiments used for experimental validation focus on 6061-T6 aluminum. The constitutive model we use for this material is a variation of the Johnson-Cook J2 plasticity model [35]. Johnson-Cook type models are commonly used in ballistic simulations, with the main appeal being its simplicity and the wide availability of constitutive parameters. The implementation we used is derived using the variational constitutive update formulation developed by Radovitzky and Ortiz [42]; Ortiz and Stainier [43] and Yang, Stainier and Ortiz [44]. The modified Johnson-

Cook flow stress is

$$Y = \sigma_0 \left[1 + \frac{\epsilon^p}{\epsilon_0^p} \right]^n \left[1 + C \log \left(\frac{\dot{\epsilon}^p}{2\dot{\epsilon}_0^p} + \sqrt{1 + \left(\frac{\dot{\epsilon}^p}{2\dot{\epsilon}_0^p} \right)^2} \right) \right] \quad (2.9)$$

with

$$\epsilon_0^p = \left(\frac{\sigma_0}{B} \right)^{\frac{1}{n}} \quad (2.10)$$

the reference plastic strain and $\dot{\epsilon}_0^p$ the reference plastic strain rate. Material properties were calibrated to match uniaxial test data. The bulk properties used for the model are listed in Table 2.2.1.

Properties	Values
Young's Modulus	$E = 72 \text{ GPa}$
Poisson's Ratio	$\nu = 0.343$
Johnson-Cook Parameter 1	$\sigma_0 = 250 \text{ MPa}$
Johnson-Cook Parameter 2	$B = 365 \text{ MPa}$
Johnson-Cook Parameter 3	$C = 0.002$
Johnson-Cook Exponent	$n = 0.04$
Reference Plastic Strain Rate	$\dot{\epsilon}_0^p = 1$

Table 2.1: Material properties for aluminum used in the modified Johnson-Cook model.

Material damage and failure is modeled with recourse to a simple continuum damage model based on a single internal damage variable [36]. The model assumes that damage is accumulated as the material continues to strain. The stress at a material point is set to zero (allowing fracture) whenever the damage variable, $D = \sum \frac{\Delta\epsilon}{\epsilon^f}$ reaches 1, where $\Delta\epsilon$ are the increments of effective plastic strain and ϵ^f is the equivalent plastic strain to failure, which can be a function of strain rate, temperature, pressure and equivalent stress in the general case. The expression used here for effective strain to fracture is given by

$$\epsilon^f = D_1 + D_2 \exp(D_3 \sigma^*) \quad (2.11)$$

where D_1 , D_2 and D_3 are fitting parameters and σ^* is the triaxiality or the ratio of σ_{ii} over the Von Mises equivalent stress. The damage variables must be calibrated to the mesh size, and fit appropriately to any available experimental data for the onset of fracture and fracture energy. In our simulations involving aluminum, we adopted reasonable damage parameters from the literature [45].

2.2.2 Brittle materials: Deshpande-Evans ceramic damage model

The Deshpande-Evans ceramic damage model was employed to model the response of the alumina used in the experimental configurations which provide validation for this simulation study [46]. The model captures the relevant constitutive response of ceramics such as elastic behavior under modest loadings and the propagation of micro cracks when subjected to tensile loadings. When subjected to high compressive loads inelastic deformation is allowed occur, which physically represents dislocation glide and twinning without cracks.

Attempts to explicitly model the microstructure of ceramics to capture inelastic behavior on the meso-scale using finite element simulations are well documented in the literature [47, 48, 49, 50, 51, 52]. Only a limited number of grains can readily be simulated in a reasonable time, as these approaches are computationally intensive, discouraging their use in engineering design applications on the macro-scale. In such situations, a continuum damage model provides a significant computational advantage by introducing a damage field defined at each material point to represent some measure of the loss of material strength at the micro-scale. This is done, for example, by representing the damage as a void volume fraction, or as a function of the density and size of micro-cracks.

The ceramic damage model used here was recently developed by Deshpande and Evans [46, 53]. The model extends the work of Ashby and Sammis [54] for modeling compressive fracture of rocks by generalizing the physically motivated damage model to include plastic deformations and improve its validity under arbitrary states of

stress for ceramics. The main assumption of the model is that micro-cracks within a unit volume can be represented by an array of uniformly sized, spaced and oriented wing-cracks. The growth of these micro-cracks are assumed to be in the worst case orientation for crack growth and are assumed to fully represent the evolution of all micro-cracks in that region. The state of these cracks is described by their density, f , their initial length, $2a$, and the angle ψ as depicted in Figure 2-1. The initial spacing between cracks is computed as $1/f^{1/3}$. It is assumed throughout that the initial flaw size and flaw spacing are related to the grain size, d , by $a = g_1 d$ and $1/f^{1/3} = g_2 d$ where g_1 and g_2 are fitting constants. A damage parameter is taken to be a function of the micro-crack state and the material loses all tensile and shear strength when the damage variable reaches 1. The compressive response is described by an equation of state which is insensitive to the state of damage.

The derivation of the constitutive model from sub-scale considerations proceeds as follows. A representative element containing an array of micro cracks is subjected to boundary conditions which correspond to the maximum and minimum principal stresses, σ_1 and σ_3 , at each material point. These conditions create Mode I stress intensities at the crack tips. Under certain stress states, the cracks are allowed to grow. The representative crack length l at a material point is initially assumed to be zero. The chosen form for the damage is $D = \frac{4}{3}\pi (l + \alpha a)^3 f$, meaning the initial damage is simply $D_0 = \frac{4}{3}\pi (\alpha a)^3 f$, where $\alpha = \cos\psi$. This form ensures neighboring cracks coalesce when $D \rightarrow 1$. The strain energy density and crack growth response is divided into three regimes, differentiated by the triaxiality of the stress state. A description of the strain energy density and crack evolution model for these three regimes is provided in Appendix A.

It is further assumed that the strain rate tensor is decomposed into elastic and plastic parts as

$$\dot{\epsilon} = \dot{\epsilon}^e + \dot{\epsilon}^p. \quad (2.12)$$

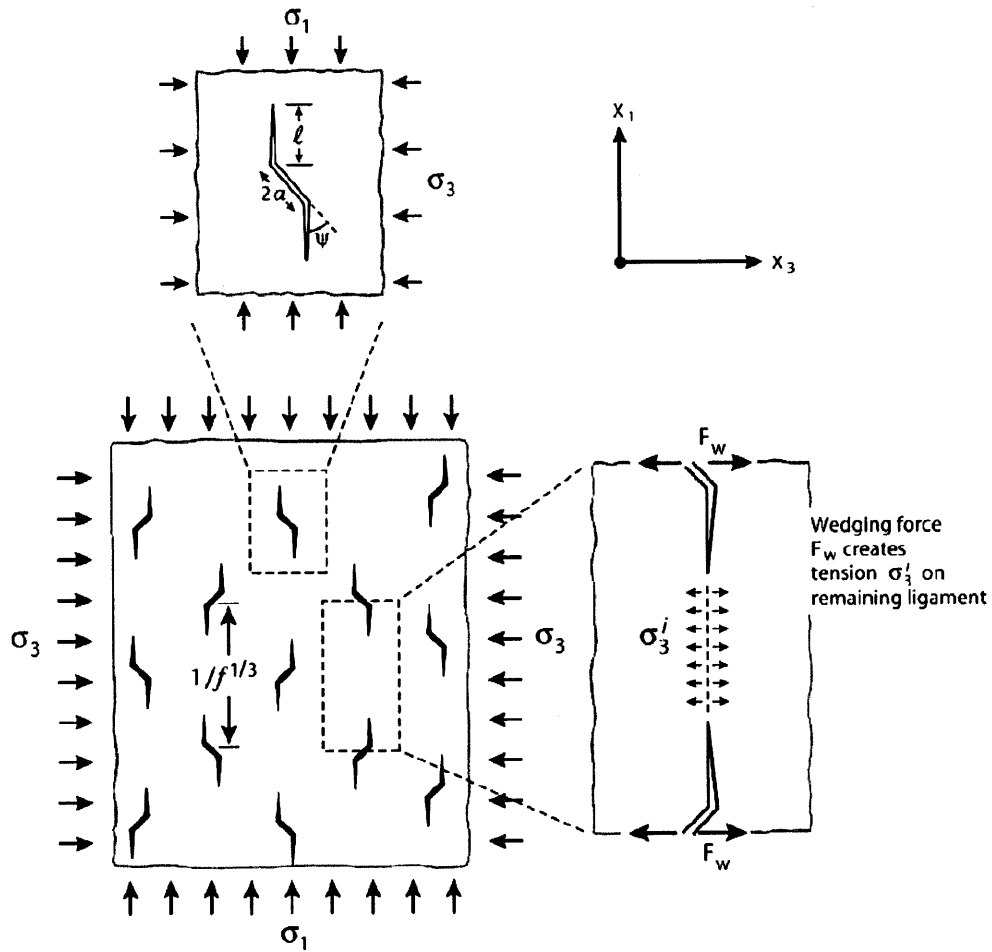


Figure 2-1: Schematic of wing-cracks motivating the Deshpande-Evens ceramic constitutive model. σ_1 and σ_3 are the maximum and minimum principal stresses (reproduced from [46])

Differentiating the strain energy density W yields the elastic strains:

$$\epsilon^e = \frac{\partial W}{\partial \sigma} \quad (2.13)$$

where W depends on the triaxiality regime (see Appendix A). A plasticity model is provided under highly compressive states of stress, when $\bar{p} = -\sigma_m$ is large. In this situation, crack growth is suppressed, and the energy dissipation mode becomes primarily plastic. A plasticity model is constructed for two distinct regimes separated by a critical strain rate $\dot{\epsilon}_t$. At low strain rates the deformation is assumed to be limited by lattice resistance and at high strain rates the dislocation velocities are assumed to be limited by phonon drag, resulting in a viscous response. The plastic strain rate is expressed:

$$\frac{\dot{\epsilon}^{pl}}{\dot{\epsilon}_0} = \begin{cases} \frac{3}{2} \frac{\sigma'}{\sigma_0} \left(\frac{\bar{\sigma}}{\sigma_0} \right)^{n-1} & \text{if } \dot{\epsilon}^{pl} < \dot{\epsilon}_t \\ \frac{3}{2} \left(\frac{\dot{\epsilon}_0}{\dot{\epsilon}_t} \right)^{(1-n)/n} \frac{\sigma'}{\sigma_0} & \text{otherwise} \end{cases} \quad (2.14)$$

where σ' is the deviatoric stress, $\dot{\epsilon}^{pl} = \sqrt{(2/3) \dot{\epsilon}^{pl} : \dot{\epsilon}^{pl}}$ is the equivalent plastic strain rate, $\dot{\epsilon}_0$ is a reference strain rate, n is a rate sensitivity exponent, $\sigma_0 = \sigma_0(\bar{\epsilon}^{pl})$ is the flow stress, and

$$\bar{\epsilon}^{pl} = \int_0^t \dot{\epsilon}^{pl}(\zeta) d\zeta. \quad (2.15)$$

The flow stress is assumed to have the form

$$\sigma_0 = \frac{\sigma_Y}{2} \left[1 + \left(\frac{\bar{\epsilon}^{pl}}{\epsilon_Y} \right)^M \right], \quad (2.16)$$

where σ_Y is the uniaxial yield strength, ϵ_Y is the equivalent plastic strain at yielding, and M the strain hardening exponent. The parameter values for the DE model used in this study correspond to that of alumina and are given in Table 2.2.2.

Properties	Values
Grain Size	$d = 38\mu\text{m}$
Initial Flaw Size Scaling Factor	$g_1 = 1.0$
Initial Flaw Size	$2a = g_1 d = 38\mu\text{m}$
Flaw Spacing Scaling Factor	$g_2 = 3$
Flaw Spacing	$1/f^{1/3} = g_2 d = 104\mu\text{m}$
Microcracks Per Unit Volume	$f = 10^{12}\text{ m}^{-3}$
Initial Damage	$D_0 = 0.01$
Shear Modulus	$G = 146\text{ GPa}$
Poisson's Ratio	0.2
Density	$\rho_0 = 3700\text{ kg/m}^3$
Mode I Fracture Toughness	$K_{IC} = 3\text{ MPa m}^{1/2}$
Reference Crack Growth Rate	$\dot{l}_0 = 100\mu\text{m s}^{-1}$
Crack Growth Rate Exponent	$m = 10$
Friction Coefficient	$\mu = 0.75$
Initial Yield Strength	4 GPa
Reference Plastic Strain Rate	$\dot{\epsilon}_0 = 0.002\text{ s}^{-1}$
Transition Equiv. Plastic Strain Rate	$\dot{\epsilon}_t = 10^6\text{ s}^{-1}$
Rate Sensitivity Exponent	$n = 10$
Strain Hardening Exponent	$M = 0.1$

Table 2.2: Material properties for alumina used in the Deshpande-Evans ceramic model.

2.3 Continuous Galerkin finite element discretization

We numerically discretized the continuum problem using conventional finite-elements. We use 10-node tetrahedral elements to avoid the “locking” problems that may arise due to plastic incompressibility constraints [55].

The finite element interpolations are defined as

$$\varphi_h(\mathbf{X}) = \sum_{a=1}^N x_a N_a(\mathbf{X}) \quad (2.17)$$

where φ_h interpolates the deformation mapping, x_a is the current coordinates of node a , and N_a are the displacement shape functions. By the principal of virtual work:

$$\left[\int_{B_0} \rho_0 \mathbf{B} N_a d\Omega + \int_{\partial B_0} \bar{\mathbf{T}} N_a dS - \int_{B_0} \mathbf{P} : \nabla_0 N_a d\Omega - \int_{B_0} \rho_0 N_b N_a d\Omega \ddot{x}_b \right] \delta x_a = 0 \quad (2.18)$$

for all virtual node displacements δx_a . This means

$$\mathbf{M}_{ab} \ddot{x}_b = \int_{B_0} \rho_0 \mathbf{B} N_a d\Omega + \int_{\partial B_0} \bar{\mathbf{T}} N_a dS - \int_{B_0} \mathbf{P} : \nabla_0 N_a d\Omega \quad (2.19)$$

where $\mathbf{M}_{ab} = \int_{B_0} \rho_0 N_b N_a d\Omega$ is the consistent mass matrix. Using the consistent mass matrix would require an expensive equation solve, so a diagonal lumped mass matrix is substituted [11].

The semi-discrete equations are integrated in time using the Newmark time stepping algorithm, whose performance and stability has been well documented [56]. The Newmark parameters were chosen for explicit time integration and second order accuracy [56], $\beta = 0$ and $\gamma = \frac{1}{2}$:

$$\mathbf{x}_a^{n+1} = \mathbf{x}_a^n + \Delta t \dot{\mathbf{x}}_a^n + \Delta t^2 \left[\left(\frac{1}{2} - \beta \right) \ddot{\mathbf{x}}_a^n + \beta \ddot{\mathbf{x}}_a^{n+1} \right] \quad (2.20)$$

$$\dot{\mathbf{x}}_a^{n+1} = \dot{\mathbf{x}}_a^n + \Delta t [(1 - \gamma) \ddot{\mathbf{x}}_a^n + \gamma \ddot{\mathbf{x}}_a^{n+1}] \quad (2.21)$$

$$\ddot{\mathbf{x}}_a^{n+1} = \mathbf{M}_{ab}^{-1} [\mathbf{f}^{ext} - \mathbf{f}^{int}]_b^{n+1} \quad (2.22)$$

where in this case $\mathbf{f}_a^{ext} = \int_{B_0} \rho_0 \mathbf{B} N_a d\Omega + \int_{\partial B_0} \bar{\mathbf{T}} N_a dS$ and $\mathbf{f}_a^{int} = \int_{B_0} \mathbf{P} : \nabla_0 N_a d\Omega$.

2.4 Adaptive remeshing

For Lagrangian problems involving unconstrained plastic flow and undergoing severe deformations, the limitations of the standard finite element discretization become apparent in situations where element distortion reduces numerical accuracy. Such situations can cause debilitating time step restrictions and can even lead to element inversion (mesh entanglement). In this case deformation gradients have negative Jacobians. Finite element discretizations modified with the additional capability of frequent adaptive remeshing between time steps have the potential to overcome these limitations for problems involving unconstrained plastic flow. Pioneering examples are the work of Marusich and Ortiz [57] for high-speed machining applications and the work of Camacho and Ortiz [55] and Yadav, *et al.* [58] for ballistic impact applications. In all these applications axisymmetric or two-dimensions approximations are used. Recent work has attempted to extend this paradigm of frequent adaptive remeshing to alleviate severe deformations and to increase fidelity to 3D simulations. This is particularly important for problems which are inherently three-dimensional in nature such as oblique penetration of a ballistic impactor [9, 59]. In this thesis, the Healmesh library is used for adaptive remeshing [59]. It is known that fundamental robustness issues exist for meshing and remeshing arbitrarily 3D domains with tetrahedral elements [60].

The remeshing approach taken here is to abandon the common strategy of completely regenerating a new mesh from scratch, with domain boundary defined by the current deformed boundary, ∂B_t . Instead, we iteratively make only local, incremental modification to the mesh, which ensures that the mesh quality is maintained or improved locally, and that the mesh continues to conform to the true boundary at all times. The algorithms used take advantage of recent advances in geometrical and topological mesh optimization and are designed to guarantee termination in finite

time. By taking this strategy, we ensure the existence of a computational mesh at all times, with the sacrifice that some situations may arise where the locally optimal mesh still contains highly degenerate elements, and local geometrical and topological changes may fail to improve the stable time step. The libraries also contain the capability for local mesh refinement. Some amount of mesh refinement appears necessary to enhance the method’s robustness and get out of the trap of local optima in mesh quality. For reasonable problems, combining these capabilities with an element refinement criterion based on finite element error estimates results in a remeshing strategy which attempts to maintain high simulation accuracy throughout. For this work, robustness is the primary concern, so the criteria to remesh and refine elements is based purely on the goal of maximizing the stable time step. In this scenario, remeshing is performed when the stable time step of the overall simulation falls below a critical threshold, or if the rate of change of the stable time step exceeds a threshold.

The final step of the process is to transfer the mechanical fields from the old mesh to the new mesh at each remeshing step. For nodal field variables such as displacements and velocities, this is performed using cubic interpolation. For internal variables the situation is somewhat more subtle, as history variable (especially ones with physical constraints such as plastic flow incompressibility) must be transferred in a manner consistent with the constitutive law and consistent with the transferred displacement fields while minimizing numerical diffusion [61]. The approach taken here is that each new gauss point simply takes its internal variable’s values from whichever gauss point was closest to it in the old mesh. This simple strategy ensures consistency with the constitutive law, has limited diffusion, and is consistent with a variational procedure for performing field and state variable transfers [61].

2.5 Contact algorithms

The type of simulations we used for our computational investigations involved the modeling of contact between impacting bodies. A continuum model for contact between bodies assumes that physical bodies never overlap, and that tractions will arise

on the boundary to exclude this possibility. Such a condition is described mathematically by an inequality constraint. This strict impenetrability constraint is often relaxed when the problem is discretized, as such a condition may cause stability issues, degrade the stable time step to magnitudes which make the simulation impractical, or require costly implicit equation solves [62]. We briefly review here some of the more common contact algorithms and their salient features.

One common class of algorithms for explicit dynamic contact are penalty contact algorithms. In these approaches, some amount of material interpenetration is allowed, but it is penalized by surface tractions [63]. The main limitation of penalty contact algorithms is their strong sensitivity to the choice of algorithm parameters which, if poorly chosen, may either lead to decreased accuracy and stability or extreme restrictions on the stable explicit time step. Another approach, which is more common for implicit dynamic computations, is exact or approximate Lagrange-multiplier methods [64], which exactly enforce non-interpenetration at the cost of significant increased computational complexity. Such an approach requires the solution of implicit systems of equations which make parallel implementations difficult. Further discussion can be found in standards texts [65, 66].

A recently proposed approach to contact, termed Decomposition Contact Response (DCR) is particularly well-suited for explicit dynamic simulations. The two key steps to this algorithm are as follows: after each time step, nodes which penetrate adjacent elements are moved by means of projection to prevent material overlap; second, momentum preserving impulses are applied such that for an elastic collision, the preservation of kinetic energy is guaranteed. The algorithm is easily adapted to handle both friction along the interfaces, as well as inelastic collisions with specified coefficient of restitution. A key feature of the algorithm is that the magnitude of the impulse transferred is independent of the time step, which means that the algorithm, unlike penalty contact algorithms, will not affect the overall stable time step. The method is introduced in the paper by Cirak and West [62] and can be derived from the framework of variational non-smooth mechanics [67].

For the range of experimental conditions studied and for the purposes of this

thesis, it suffices to consider the impacting object as a rigid body. A modification of the DCR algorithm was derived and implemented to handle the rigid body impact of a solid sphere on a finite element mesh. A derivation of this algorithm follows.

We consider the total momentum of the interacting system \mathbf{P}_c , which consists of the rigid body and the nodes which come into frictionless contact with the body (extensions including friction are possible, but will not be discussed here):

$$\mathbf{P}_c = m_{sph} \mathbf{v}_{sph} + \sum_{i=1}^n m_i (\mathbf{v}_i \cdot \mathbf{N}_i) \mathbf{N}_i \quad (2.23)$$

where \mathbf{P}_c is the total interacting momentum of the mass in contact, \mathbf{v}_{sph} and m_{sph} are the rigid sphere's velocity and mass, \mathbf{v}_i and m_i are the velocity and mass of the i^{th} node, \mathbf{N}_i is the normal direction to the sphere for the i^{th} node, and n is the total number of nodes which penetrated the surface of the rigid sphere during the previous time step. This equation ignores the component of momentum for each node tangent to the surface of the sphere. The algorithm is based on the assumption that the total momentum of the interacting system \mathbf{P}_c remains constant. This guarantees conservation of momentum for the entire system.

In addition to requiring conservation of momentum, we also require conservation of energy for the case when the coefficient of restitution is 1. The other extreme is for a coefficient of restitution equal to 0. In this case we want the component of velocity for each node normal to the surface of the sphere to be equal to the component of velocity of the sphere in that direction. This is the case where two objects collide plastically and “stick” in the direction normal to contact, but slide without friction in the perpendicular direction. Between these two extremes, we assume that the velocity change depends linearly on a coefficient of restitution, $0 \leq C_R \leq 1$. This can be accomplished by updating the velocity for each node as

$$\mathbf{v}_i \leftarrow [(\bar{v}_i - v_i) + C_R (\bar{v}_i - v_i)] \mathbf{N}_i \quad (2.24)$$

where $\bar{v}_i = \bar{\mathbf{v}}_c \cdot \mathbf{N}_i$ is the average velocity of the system in the direction \mathbf{N}_i , $v_i = \mathbf{v}_i \cdot \mathbf{N}_i$ is

the initial velocity magnitude of i^{th} node in the direction \mathbf{N} , $\bar{\mathbf{v}}_c = \frac{\mathbf{P}_c}{M_c}$ is the momentum weighted average velocity of the system, and $M_c = m_{sph} + \sum_{i=1}^n m_i$ is the total mass of the interacting system. The velocity of the sphere is updated similarly, such that the total momentum of the system is conserved. The algorithm was extended to a parallel MPI implementation, which uses MPI reduction commands to determine and communicate the total interacting system's mass and momentum across all processors.

The algorithm then proceeds as follows:

- At each time increment, determine all the nodes which penetrate the rigid sphere projectile.
- Compute the normal direction for each node penetrating the sphere, as measured from the center of the sphere. Project all the nodes to the surface of the sphere using closest point projection along this normal direction.
- Compute the total momentum of the interacting system, ignoring friction. This requires summing the momentum of the sphere together with the component of momentum for each node projected normal to the surface of the sphere.
- With specified coefficient of restitution, exchange momentum between the nodes and the sphere by simultaneously and instantaneously changing their velocities according to equation 2.24.
- Continue with the time step. Update nodal coordinates using the continuum dynamic discretization and the sphere's coordinates using second order explicit time integration.

This rigid body (DCR) contact algorithm has proved successful in modeling the impact of a rigid sphere on a finite element mesh. While in some situations the details of the sphere's inelastic deformation become quite important, as a first attempt to capture the primary physics of the impact event, this approach has shown promise. Momentum and energy conservation with $C_R = 1$ was verified for the implementation. This algorithm was successfully used in applications which will be discussed in Chapter 3.

Chapter 3

Finite element simulations of ceramic impact using damage models

Applications for ceramic armor are prevalent in defense applications due to mechanical properties of ceramics such as high strength in compression and hardness. After failure, ceramic are still able to maintain compressive strength and tend to exhibit bulking, which is an increase in volume. The main drawback of ceramics is that they are very brittle and relatively weak in tension [68]. Ballistic impact experiments of ceramic targets typically exhibit a variety of dissipative mechanisms including radial cracks, conical cracks, a comminuted zone underneath the impact site, and even lattice plasticity. Ballistic impact of ceramic targets simulated using finite elements or Lagrangian particle methods have been well documented in the literature. Holmquist and Johnson [68] calibrated their previous damage model for brittle materials [69] to predict the outcome of long rod penetration into confined ceramic. They were able to predict material defeat and the transition to dwell at higher impact velocities as observed in the experiments of Lundberg, *et al.* [70]. Ballistic impact of silicon carbide has also been simulated [71] using the brittle damage law of Johnson, Holmquist and Beissel [72]. These simulations were conducted primarily in an Eulerian framework, occasionally coupled to Lagrangian finite elements. The approach succeeded in pre-

dicting radial crack patterns as well as dwell and penetration observed experimentally. Fawaz, *et al.* [73] perform 3D simulations showing both normal and oblique impact of ceramic armor systems. These computations were performed with a commercial code using element erosion to capture failure/fracture and handle the severe deformations. The results show reasonable qualitative agreement with the experimental trends such as residual velocity vs. plate thickness for a fixed impact velocity.

3.1 High speed impact of ceramic tiles

As an initial validation for the framework described in Chapter 2, we used the Deshpande-Evans ceramic model [46] applied to the problem of a spherical projectile impacting a confined ceramic tile. The materials properties used for the simulated ceramic are listed in Table 2.2.2.

We qualitatively compare our results with the experimental results performed by Zok [74]. The experimental setup is shown in Figure 3-1 and consists of a confined ceramic tile with a width and length of 50.8 mm and a thickness of 12.0 mm confined in an elastic medium. A spherical steel projectile of radius 3.77 mm is impacted into the center of the target at velocities ranging from 288 m/s to 750 m/s [74].

Experimental results showing both front-face and back-face crack patterns of the ceramic after impact at velocities of 288 m/s and 588 m/s as shown in Figure 3-2. Front-face images are on top, and mainly depict radial crack patterns. Back-face images are on the bottom and show radial cracks as well as indications of conical shaped cracks which originate at the impact site. Through slice images for these cases are shown in Figure 3-3 and clearly show the conical crack patterns.

3.1.1 Simulation setup

The projectile is modeled as a rigid sphere with radius 3.77 mm and density 7800 kg/m³. The ceramic tile is modeled with a finite element mesh 12.0 mm in height and with a square base of length 50.8 mm. The constitutive response is governed by the Deshpande-Evans ceramic model, with parameters give in Table 2.2.2, which

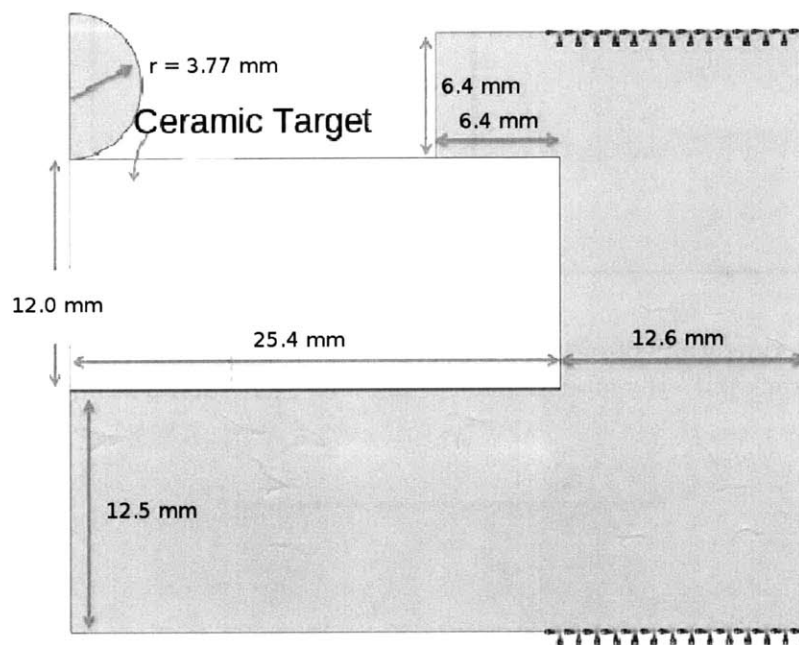


Figure 3-1: Schematic of experimental setup for confined ceramic tile impact (obtained from [74])

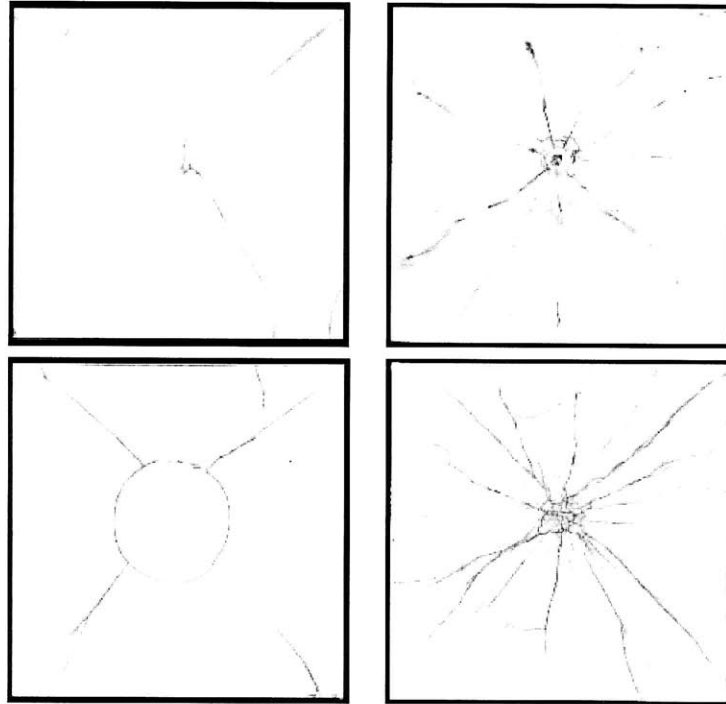


Figure 3-2: Experimentally observed post-mortem ceramic front-face (top) and back-face (bottom) crack patterns after impact at 288 m/s (left) and 588 m/s (right) [74]

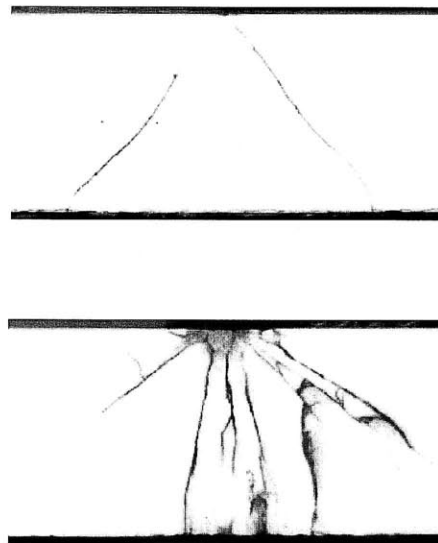


Figure 3-3: Experimentally observed through slice of post-mortem ceramic tile impacted at 288 m/s (top) and 588 m/s (bottom) [74]

were calibrating using a 2D axi-symmetric model [74]. The number of elements used varied from 200,000 to 1.6 million elements for the coarse and fine simulations respectively. The rigid body decomposition contact response algorithm described in Chapter 2 was used to model the impact of the rigid sphere into the ceramic tile. The ceramic tile was completely constrained along its horizontal edges, but remained unconstrained along the bottom and top surfaces. Reasonable good qualitative agreement was achieved without modeling the exact experimental confinement. Adaptive remeshing was not used for these simulations. The simulations were executed in parallel using 24 processors. The simulation setup for one of the finite element meshes, with the mesh partition indicated by color, is shown in Figure 3-4.

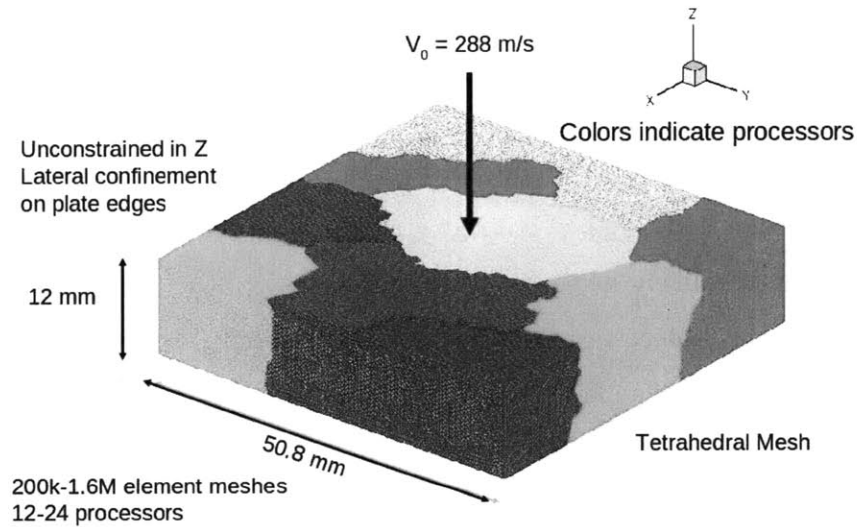


Figure 3-4: Finite element mesh and simulation setup showing processor allocation

3.1.2 Simulation results

A few snapshots at different time steps for an initial projectile velocity of 288 m/s using the coarsest mesh are shown in Figures 3-5 to 3-7. The four views show: contours of damage on a cross section of the plate along a diagonal (top left); contours of

damage on the back-face (top right); contours of mean stress on the top-face (bottom left); and contours of von Mises stress on the top face (bottom right). Snapshots at different time steps with the same setup, but using the refined mesh, are shown in Figures 3-8 to 3-10.

Both levels of refinement show the propagation of stress waves emanating from the impact site on the top-face and eventually reflecting off both the fixed and free surfaces. The simulation results show that the damage crack features first emerge on the back-face. This can be attributed to the tensile release wave which results from the reflection of the initial impact compressive wave off the back-face. The softening response, which follows from the increase in damage, localizes into a discrete number of cracks which propagate outward from the center of the back-face. Both levels of refinement show the development of a conical crack pattern in the cross sectional view, though this feature is clearer in the fine mesh. The shape of this feature can be attributed to the fact that as the tensile wave propagates off the back-face, the maximum principal stress direction would be oriented roughly at 45° . Due to the transients, the confinement, and the fact that the tensile wave is not a perfect plane wave, the conically shaped damage crack localize at a sharper angle than 45° . This cone angle will likely depends strongly on, among other things, the boundary conditions and the aspect ratio of the tile. To summarize, the simulations were successful in capturing the main features of the experimental results, specifically the radial crack patterns emanating from the impact site, as well as the conically shaped crack patterns which originate at the top of the impact region and propagate through the thickness of the specimen.

3.1.3 Discussion

Despite the apparent success of these simulations, difficulties with the model remain. The first issue, which is fundamental to nearly all damage models, is the significant mesh dependence of the resultant damage patterns. In the continuum limit damage models are ill-posed and often require the addition of a physical length scale to regularize [39]. As the discretization is refined, the damage zones localize to a

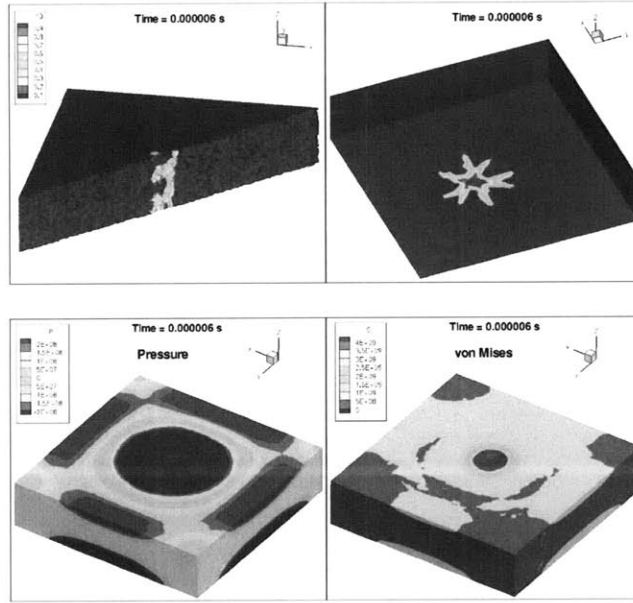


Figure 3-5: Ceramic tile impact simulation: snapshot of damage on a cross section (top left), damage on the back-face (top right), mean stress on the top-face (bottom left), and von Mises stress on the top-face (bottom right) for the coarse mesh at $t = 6\mu\text{s}$

smaller region and less energy is dissipated. In these simulations, the length scale is provided by the average element size. As a demonstration of this issue, we refined our computational mesh uniformly by subdividing each tetrahedron into 8 elements. A comparison of the simulation results for coarse and fine meshes is shown in the Figures of Section 3.1.2. A direct comparison of the contours of damage for the two resolutions is shown from different perspectives in Figure 3-11. It is observed that by increasing the spatial resolution of the computational domain by a factor of 2 in each direction, the size of the predicted cracks decreases, while the number of total cracks roughly doubles. If the mesh were refined further, the crack zone sizes would continue to shrink, resulting in decreased energy dissipation. Simulations at higher impact velocities proved difficult due to stability issues with the constitutive law and mesh entanglement under the projectile.

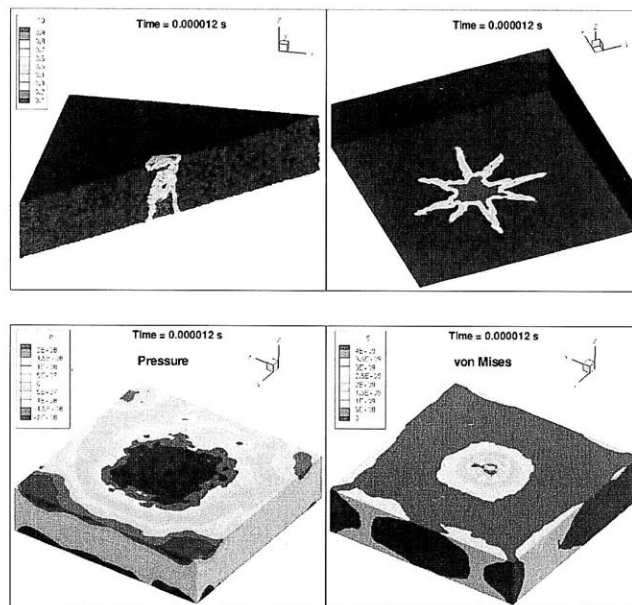


Figure 3-6: Ceramic tile impact simulation: snapshot of damage on a cross section (top left), damage on the back-face (top right), mean stress on the top-face (bottom left), and von Mises stress on the top-face (bottom right) for the coarse mesh at $t = 12\mu s$

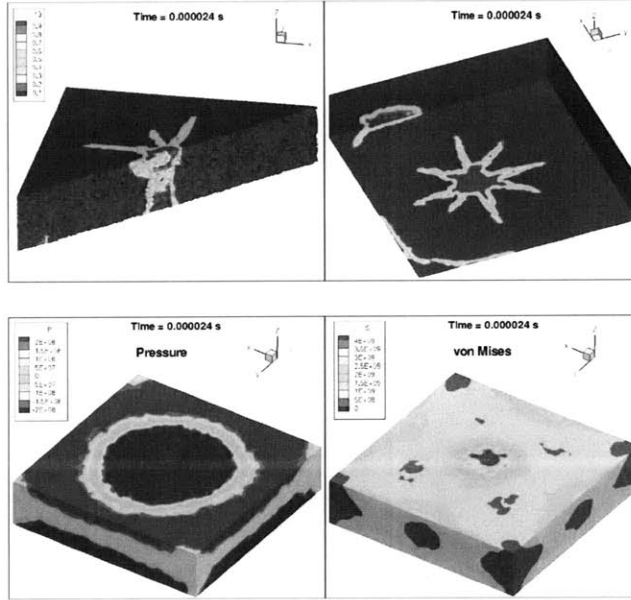


Figure 3-7: Ceramic tile impact simulation: snapshot of damage on a cross section (top left), damage on the back-face (top right), mean stress on the top-face (bottom left), and von Mises stress on the top-face (bottom right) for the coarse mesh at $t = 24\mu s$

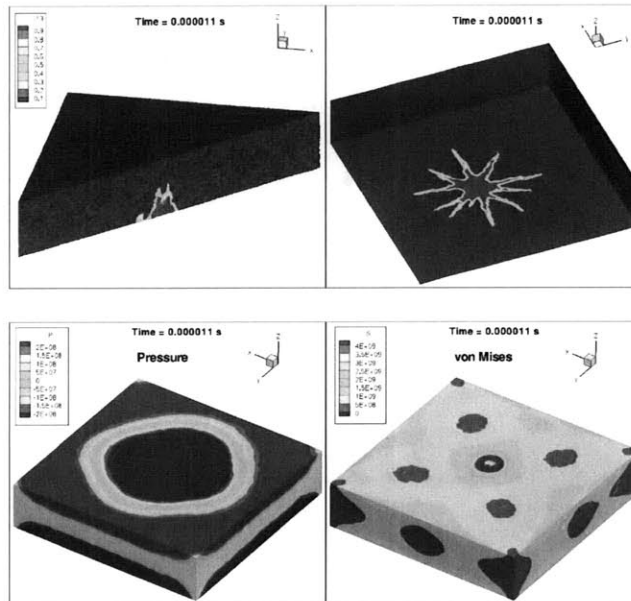


Figure 3-8: Ceramic tile impact simulation: snapshot of damage on a cross section (top left), damage on the back-face (top right), mean stress on the top-face (bottom left), and von Mises stress on the top-face (bottom right) for the fine mesh at $t = 11\mu s$

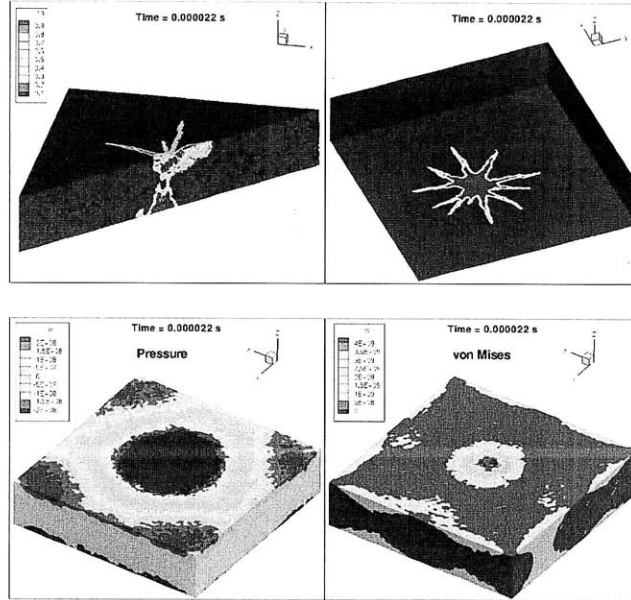


Figure 3-9: Ceramic tile impact simulation: snapshot of damage on a cross section (top left), damage on the back-face (top right), mean stress on the top-face (bottom left), and von Mises stress on the top-face (bottom right) for the fine mesh at $t = 22\mu\text{s}$

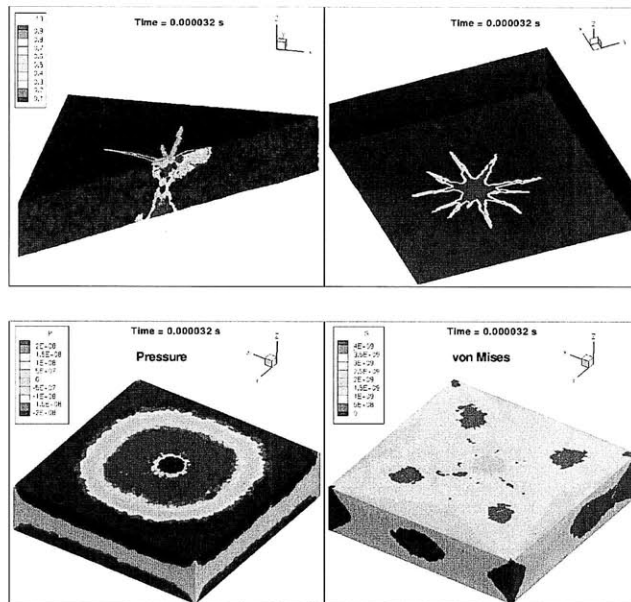


Figure 3-10: Ceramic tile impact simulation: snapshot of damage on a cross section (top left), damage on the back-face (top right), mean stress on the top-face (bottom left), and von Mises stress on the top-face (bottom right) for the fine mesh at $t = 32\mu\text{s}$

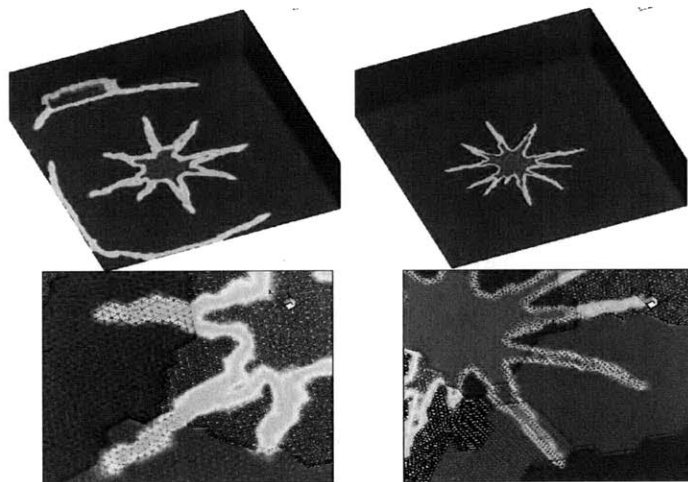


Figure 3-11: Mesh-size dependency of damage contours on back face of ceramic tile

3.2 Long-rod penetration of confined ceramic target with finite elements using adaptive remeshing

As a second test of the framework described in Chapter 2 with adaptive remeshing, we use the Deshpande-Evans ceramic model [46] to simulate long-rod penetration into confined ceramic. These numerical tests were motivated by the experimental results of Lundberg and Lundberg [1], who studied the penetration of tungsten rods into different silicon carbide materials. The experiments demonstrated a transition between interface defeat, dwell on the interface and impactor penetration as the impact velocity was varied. The material properties we used for alumina were not fitted to the actual material in the experiments as the investigation at this stage is purely qualitative and aimed at understanding the limitations of the numerical methods, with less emphasis on the physical fidelity. The parameters used for the ceramic are give in Table 2.2.2, while the tungsten rod was modeled with a simple J2 plasticity law. Snapshots from these experiments, adapted from [1], depicting X-ray images of the ceramic at different times after impact are shown in Figure 3-12. The experimental setup had a tungsten projectile impacting confined SiC-HPN at 1578 m/s (top) and 1749 m/s (bottom). For the lower impact velocities, it is clear that the projectile failed to penetrate the surface of the confined ceramic, but there is evidence of dwell, with material flowing radially along the interface. At the higher impact velocities the projectile managed to completely penetrate the surface.

The transition from dwell to penetration is demonstrated by plotting the penetration depth vs. time for a variety of impact velocities, as shown in Figure 3-13 [1] for SiC-HPN. These results show that up to a certain velocity, the rod completely fails to penetrate into the ceramic. However, when the velocity is increased from 1613 m/s to 1636 m/s there is a sudden jump in the depth of penetration. An alternative way to demonstrate this effect is by measuring the residual velocity just after penetration vs. the impact velocity. This is shown in Figure 3-14 for SiC-HPN [1]. The penetration

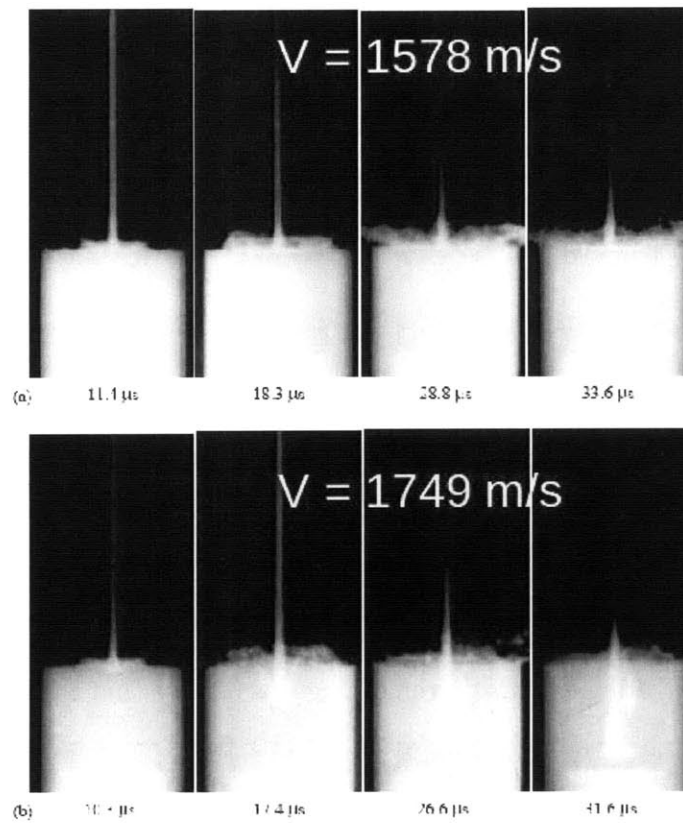


Figure 3-12: Long-rod penetrator impacting confined silicon carbide: transition from dwell to penetration [1]

velocity makes a significant jump after 1636 m/s, then only increases linearly with impact velocity at higher impact velocities.

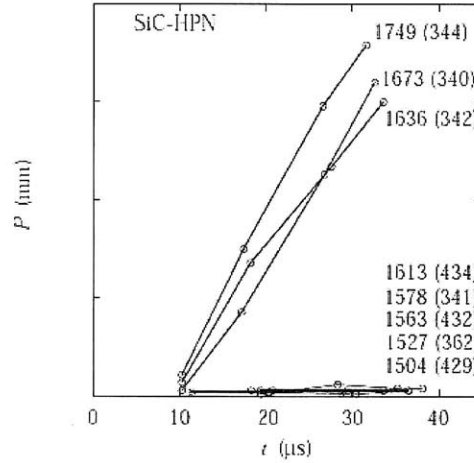


Figure 3-13: Penetration depth vs. impact velocity for long-rod penetrator impacting confined silicon carbide [1]

3.2.1 Simulation setup

Simulations were performed which attempted to emulate the conditions and geometry of the Lundberg experiments, with the goal of correctly predicting a sharp transition from dwell to penetration. Adaptive remeshing was used so that the simulations could progress long enough for a final penetration velocity to be measured. The goal of such an approach is to eliminate mesh-induced distortion, resolve fine-scale features via mesh refinement, and improve model accuracy. The benefit of the specific remeshing algorithm used is that it only performs local mesh changes, eliminating the need to generate an entirely new mesh from scratch each time a remeshing step is required. In many applications, mesh adaptation and refinement is based on *a posteriori* error estimates [42]. However, the critical limitation here is the very ability to maintain a correctly defined element mesh topology by avoiding element inversion. Consequently, our adaptive remeshing criterion is based solely on local element quality metrics and their rate of degradation. This approach strives to preserve high quality elements and to prolong the simulation time. Unfortunately, even with remeshing, the robustness of

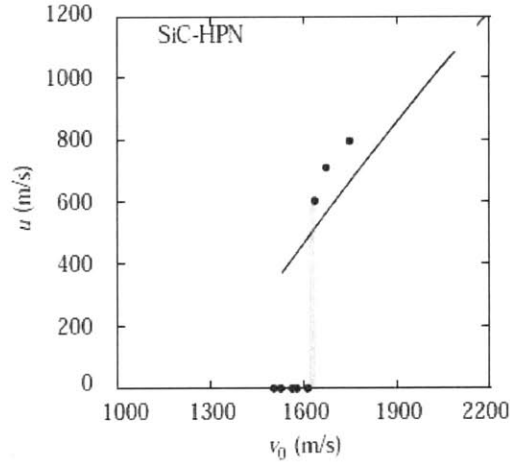


Figure 3-14: Penetration velocity vs. impact velocity for long-rod penetrator impacting confined silicon carbide [1]

the framework is limited. After only a few micro-seconds of simulation time, either the stable time step decreased steadily to zero or some of the elements inverted, killing the simulation. Several potential improvements were attempted including: adjusting the contact parameters, changing the contact algorithm, and using artificial viscosity [38]. New heuristics in the adaptive remeshing algorithm were developed which improved simulation duration, but did not completely eliminate the robustness issues.

The geometric set up for these simulation had a 10 mm long tungsten rod with a 1 mm radius impacting a ceramic target, 20 mm long with at 10 mm radius. Both the projectile and the target were discretized with finite elements. A contact algorithm handled the coupling between the discretized domains. For this initial investigation the true confinement boundary conditions were not modeled. Typically, the ceramic target's confinement was modeled as being fully constrained on the sides, but not on the bottom. Ideally the actually confining material would be modeled, but as an initial evaluation of the remeshing capabilities, this complication was ignored. When the bottom surface was also confined, there was not enough room for the penetrator to displace the ceramic significantly, so interface defeat occurred at much higher velocities.

Three different simulations were attempted. The first used an impact velocity of

1000 m/s for the projectile. In this case the contact algorithm we used was based on a master-slave approach [10]. When a slave node penetrates into the master mesh, the slave node is projected to the master mesh's surface and momentum is exchanged by the algorithm between time steps. This algorithm was sufficient for low impact velocities, but resulted in unphysical and severe distortion on the surfaces of the meshes at higher velocities. These distortions ultimately caused the simulations to fail early. The second and third simulations used an impactor velocity of 1600 m/s. The original Cirak and West decomposition contact response algorithm [62] was used for these higher velocity impact simulations. This alternative contact algorithm led to higher quality mesh surfaces during contact as compared with the master-slave approach, but element failure was still inevitable due to the large plastic flows. The third simulation setup was identical to the second, except that a finer finite element mesh was used for both the target and the projectile.

3.2.2 Simulation results

Snapshots from the first simulation, which used a projectile velocity of 1000 m/s, depicting contours of damage are shown in Figure 3-15. In this simulation, the side of the target was left fully unconstrained. Radial crack patterns are clearly present, and can be attributed to stress release waves propagating off the surface of the ceramic target. Even unconfined, the projectile was defeated by the ceramic target. The slight mushrooming of the impacting penetrator is an indication of dwell. Remeshing was used primarily in projectile as it deformed during impact.

Snapshots from the second simulation with the improved contact algorithm are shown in Figure 3-16. The impact velocity in this case was 1600 m/s and the sides of the target were fully constrained. Snapshots from a refined simulation using the same setup are shown in Figure 3-17. For both of these simulations, the projectile's velocity was high enough for it to penetrate into the ceramic target. The fine simulation was sufficiently resolved to capture radial crack patterns emanating from the source of impact. The coarse simulation is clearly under-resolved as the cracked and comminuted zone beneath the impactor shows just a large region of damaged mate-

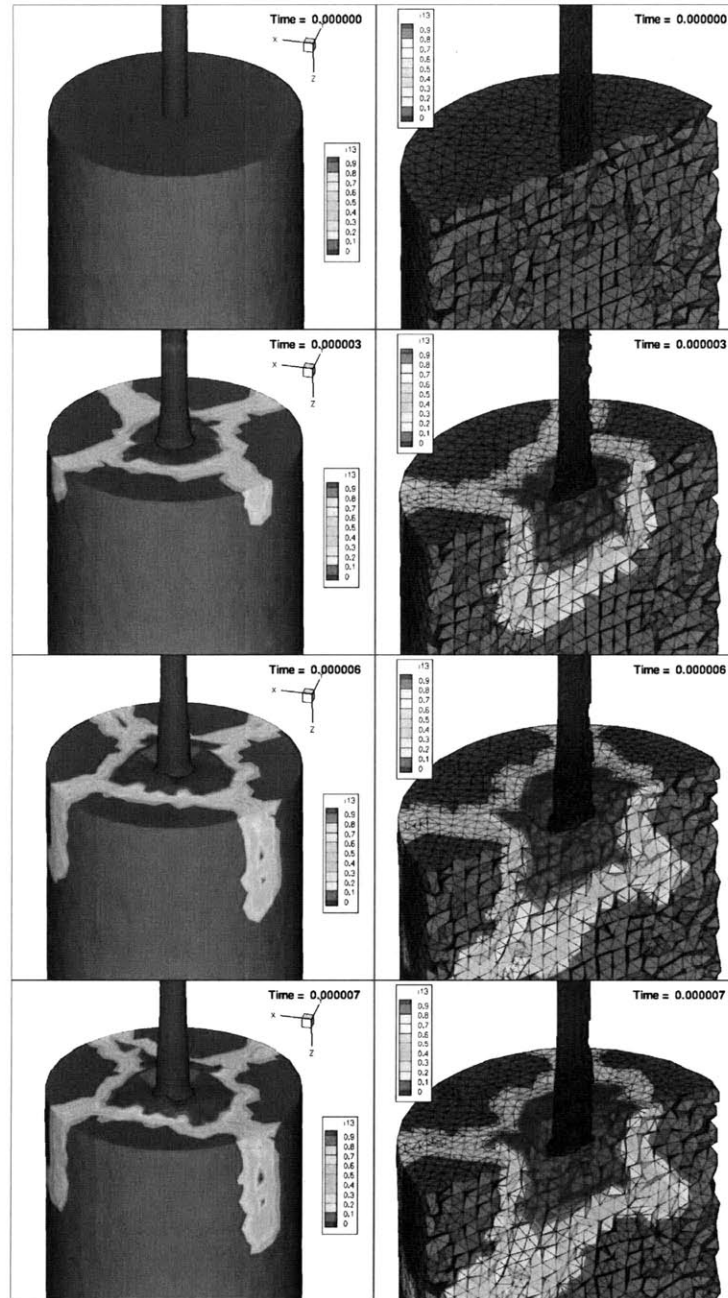


Figure 3-15: Damage contours of ceramic target impacted at 1000 m/s

rial. The refined simulation was unable to proceed as far in computation time as the coarse simulation, which can be attributed to the greater degree of softening which occurs when the finer mesh localizes.

All of these simulations were performed in serial, as remeshing algorithms are difficult to parallelize and that task has been left for the future. A remeshing step is performed roughly every 100 time steps, unless the algorithm detects the additional need to remesh due to rapid element quality degradation. Frequent remeshing is required, as the field variable transfer accuracy will suffer otherwise. The run time for these simulation was quite long, with the coarse simulations taking approximately 5 days to complete, and the fine simulation taking approximately two weeks. The expense of this approach is primarily due to the inevitable decrease in stable time step, the additional computation cost of remeshing, and the fact that the simulations could only be run on a single processor.

Direct comparisons between the low velocity and high velocity simulation results are somewhat meaningless, as both the boundary conditions and the contact algorithm was changed. However, the results do exhibit both dwell at the lower impact velocity, and penetration at the higher velocity. This methodology has not yet proven successful in predicting the precise transition velocity from dwell to penetration.

While adaptive remeshing is an appealing approach for overcoming the limitations of the finite element method, fundamental limitations on the ability to remesh arbitrary 3D domains constrain its robustness. At present, this methodology is best suited for serial computations, as highly scalable parallel implementations remains a challenge. The difficulties faced when simulating high velocity impact problems indicate that there is a need for a Lagrangian computation method which does not require a topologically well defined mesh, adaptive remeshing, or field transfers. Such a strategy, based on a discretization of the new continuum theory of peridynamics, is explored in Chapter 4.

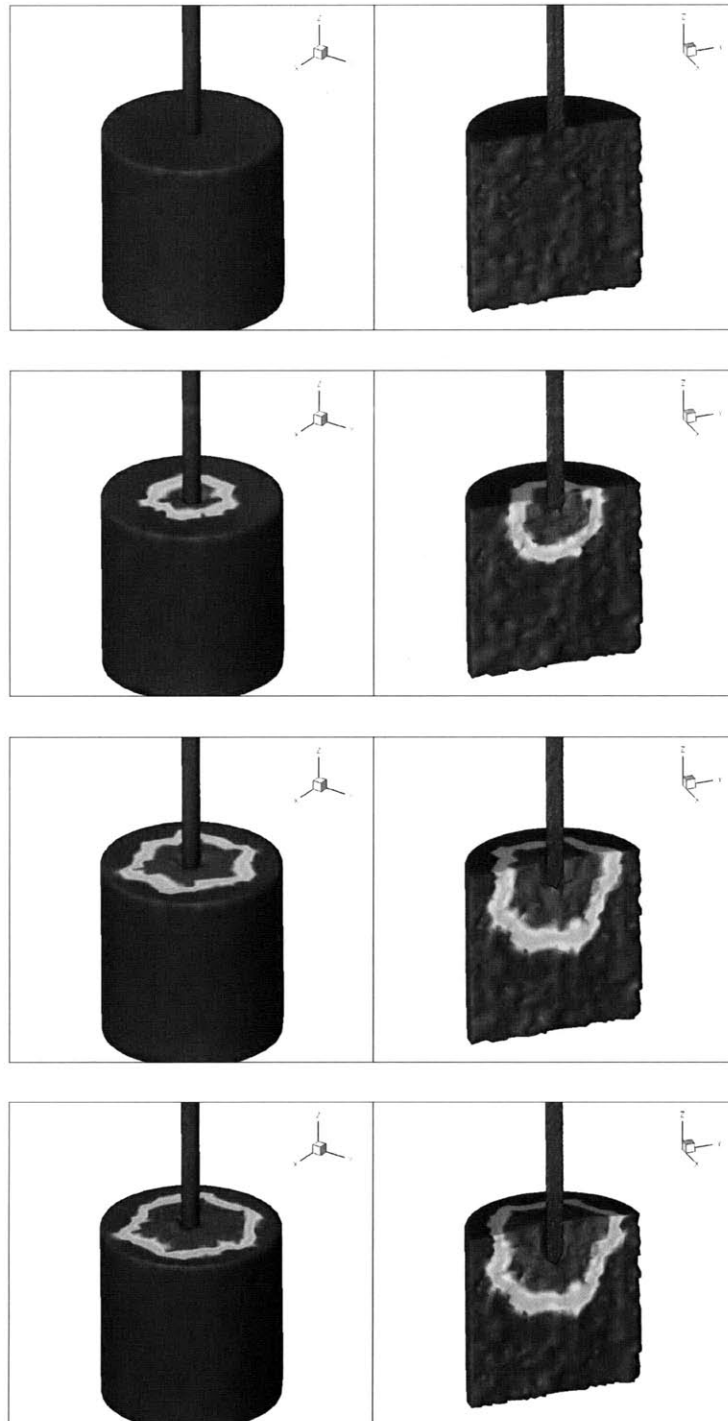


Figure 3-16: Damage contours of ceramic target impacted at 1600 m/s: coarse mesh

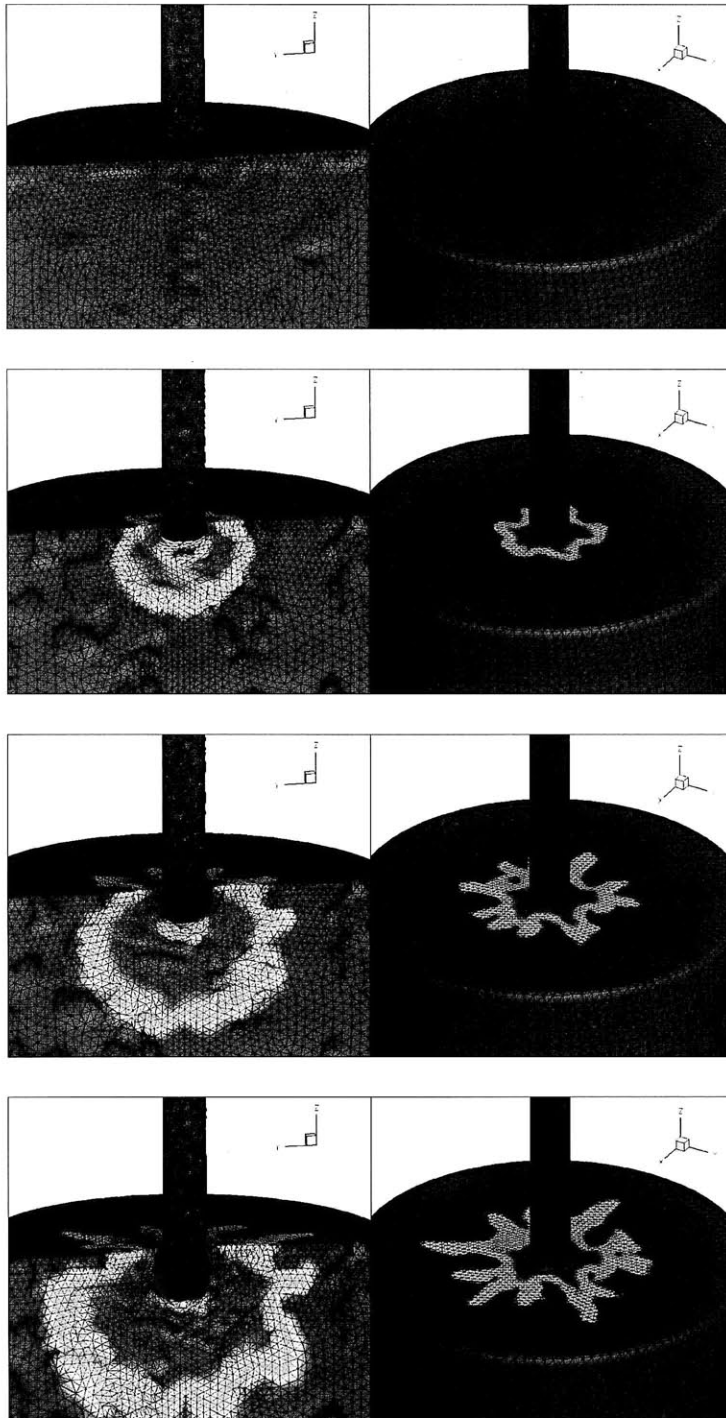


Figure 3-17: Damage contours of ceramic target impacted at 1600 m/s: fine mesh

Chapter 4

Peridynamics

Peridynamics is a continuum theory based on a generalization of the local stress assumption of classical continuum mechanics to allow for forces acting at a distance, thereby introducing a length scale to the continuum description. The typical assumption of local stress states in a material limits the interaction of materials points to immediate neighbors in direct contact with each other. The alternative approach taken in peridynamics is a continuum theory based on integral equations, which “sum” force contributions from material points acting at a distance. The material behavior is determined by these non-local interactions, where the interaction forces are taken to be functions of the deformation within a finite neighborhood of material. In a sense, the peridynamic theory more closely resembles molecular dynamic interactions where forces act on atoms at a distance. All continuum theories are ultimately macro-scale homogenized approximations of these atomistic interactions. The idea for peridynamic was first proposed by Silling in 2000 [34]. The initial model was restricted to elastic materials which in three dimensions have a Poisson’s ratio, $\nu = 0.25$. This initial theory laid the foundation of what is now known as bond-based peridynamics, which only considers pairwise interaction between distinct material points. A more recent extension of the theory, name state-based peridynamics, was introduced by Silling *et al.* in 2007 [2] and allows for more general interaction potentials and interaction forces between distinct material points.

Classical continuum constitutive laws with either plastic softening or damage suffer

from the emergence of negative tangent moduli and therefore imaginary wave speeds [39]. Boundary value problems with such a constitutive response are mathematically ill-posed, as material softening will localize to an infinitesimal region. Because finite element discretizations contain their own length scale, the element size, the localization in finite element simulations only occurs down to this scale. This means convergence for classical softening models is impossible and the localized regions continue to shrink as the mesh is refined. To solve this issue, a physical length scale must be introduced into the constitutive description using non-local theories. Such theories are broadly grouped into two categories: weakly non-local and strongly non-local [39]. Strain gradient and higher order gradient theories such as those of the Mindlin variety [75] are examples of weakly non-local theories, as the non-local effects are approximated by evaluating higher order gradients locally. Peridynamics, on the other hand, is a strongly non-local theory due to its integral formulation and its explicit inclusion of forces acting at a distance. The peridynamic theory accepts non-local interactions from the onset, thereby providing a physical length scale to regularize the continuum description.

One further complication of the theory, compared to classical elasticity theories is the complicated dispersion relation which results from the non-local interactions. The issue also arises in other non-local models including higher order gradient theories [75] and strongly non-local theories [76, 77]. For a classical elastic material, the wave speed is independent of the wave number, but this is not in general true for peridynamics. However, it is known that all real materials exhibit complicated dispersion behavior at sufficiently small wavelengths [77]. It has been shown that specific peridynamic models are able to reproduce the “exact” elastic dispersion relation for sufficiently small wave number, or equivalently, sufficiently small peridynamic horizon length [78, 77].

The discretization of peridynamics leads to a particle based method which is similar to other meshless discretizations of classical continuum mechanics in that the internal forces are work conjugate to particle displacements. The main difference is that the peridynamic discretization uses no elements, basis functions, kernels, or

ad hoc differencing techniques and therefore results in a truly meshless, elements free, mesh-free, node-based, particle method for approximating problems in continuum mechanics. Owing to recent advances [2, 79], the discretization of peridynamics is accompanied with a strong theoretical background for guiding the construction of numerical schemes which directly satisfy conservation laws, but can still utilize classical constitutive models, such as viscoplasticity. Of historical interest is a similar meshless formulation which comes from the physics-based computer animation community [80]. The similarity is that all state and internal variables are stored at particle locations and their internal forces are derived to be work conjugate to the particle displacements.

Owing to the integral formulation and the relaxed continuity requirements, fracture and fragmentation can be introduced in a natural manner without the need for cohesive elements or other devices commonly used in classical continuum discretizations [8]. As no gradient terms arise in the formulation, the equations are still valid in the presence of discontinuities such as cracks and phase boundaries. This eliminates the need for additional constitutive assumptions at the interface. This benefit is not without its own complications, as it is accompanied with the additional burden of incorporating additional constitutive information such as fracture criteria directly into the continuum formulation. Significant effort has already gone towards developing and utilizing the advantages of the peridynamic formulation for modeling fracture [81, 82, 83, 84, 85, 86]. The convergence properties of bond-based peridynamics for modeling crack propagation was numerically investigated by Bobaru, *et al.* [87]. This investigation helped establish the notion that both the spatial resolution of the discretization, along with the length scale introduced by the peridynamic formulation must be considered when evaluating the properties of a peridynamic discretization.

Since its inception, peridynamics has already been used in a variety of different continuum mechanics applications. These include membrane and fiber models [81], phase transitions [88], inter-granular fracture [83], and heat transfer [87]. An implementation of peridynamics using traditional finite element codes, via beam elements, has also been presented in [89]. A bond based formulation has also been implemented

in a molecular dynamics code, LAMMPS [84]. Analytical results have shown the dependence of the non-local effect of the bond-based model on the material response for simplified 1D scenarios [90, 78]. Peridynamic formulations of continua have also demonstrated their relevance for meso-scale modeling of material response [83]. In this respect, peridynamics may provide a means of bridging length scales within a multi-scale paradigm.

Several results exist on the mathematical properties of the bond-based theory, including well-posedness and convergence [91, 92]. In particular, it has been proved that elastic bond-based peridynamics converges to classical elasticity for the special case where the Poisson's ratio, $\nu = 0.25$ [92]. It has also been shown that there is a correspondence between strain gradient elasticity and elastic peridynamics [92]. This comparison between the theories is only applicable in situations where the displacement fields are sufficiently smooth to permit a classical interpretation, and is no longer meaningful near strong discontinuities.

The recent landmark improvement provided by state-based peridynamics has allowed the theory to be extended to a much broader class of constitutive models [2]. In particular, it allows for inelastic materials and materials with Poisson's ratio other than 0.25 to be modeled. The ability of this state-based peridynamic theory to model viscoplasticity has been demonstrated and validated using a Taylor impact test [79]. This has provided evidence that a peridynamics particle method for modeling large unconstrained plastic flow may be able to overcome many of the traditional issues associated with plastic flow modeled using finite element methods.

4.1 Bond-based peridynamics

In the original peridynamic formulation the classical equation of conservation of linear momentum is replaced by the bond-based peridynamic equation of motion:

$$\rho \ddot{\mathbf{u}}[\mathbf{x}, t] = \int_B \mathbf{f}(\mathbf{u}[\mathbf{x}', t] - \mathbf{u}[\mathbf{x}, t], \mathbf{x}' - \mathbf{x}) dV_{\mathbf{x}'} + \mathbf{b}[\mathbf{x}, t] \quad (4.1)$$

where the ρ is the density of the material at the point \mathbf{x} in the reference configuration, \mathbf{u} the displacement field, \mathbf{b} is a prescribed body force density, and \mathcal{B} the domain of the body under consideration in the reference configuration. Each pair of particles in the body interacts through the vector valued function $\mathbf{f}(\mathbf{u}[\mathbf{x}', t] - \mathbf{u}[\mathbf{x}, t], \mathbf{x}' - \mathbf{x})$. The integral term should be interpreted as the force per unit reference volume which is due to its interaction with other particles in the body. It is typically assumed that the function \mathbf{f} has spherical compact support of radius δ centered at \mathbf{x} . This peridynamic horizon radius can be tuned to capture the relevant physical length scale. In the limit of this radius going to zero, the theory in 3D reduces to classical elasticity with $\nu = 0.25$ [92].

While advantageous for problems involving non-local effects and discontinuities, bond-based peridynamics is limited to pairwise interactions via central acting forces. This leads to the limitation on the Poisson's ratio and means that any plasticity formulation will require permanent volumetric deformations. This results in a strong limitation on the variety of materials which can be accurately modeled using the theory. To address these issues, Silling *et al.* developed a new formulation of peridynamics called state-based peridynamics [2]. Their formulation is a significant generalization of the peridynamic framework, which allows the response of the material at a given point to depend on the collective deformation of all points in the neighborhood. In the following section we describe the state-based formulation.

4.2 State-based peridynamics

4.2.1 Peridynamic states

Let \mathcal{D} denote a spatial domain centered at the origin in \mathbb{R}^3 . A peridynamic vector state is a mathematical object, $\underline{\mathbf{A}}$, defined by the mapping

$$\underline{\mathbf{A}}(\boldsymbol{\xi}) : \mathbb{R}^3 \rightarrow \mathbb{R}^3 \quad (4.2)$$

where the underscore is used to indicate a peridynamic state. A peridynamic vector state is an infinite dimensional object, with the mapping defined for all bonds (vectors) $\underline{\xi} \in \mathbb{R}^3$.

The bond, $\underline{\xi} \in \mathbb{R}^3$, between two material points in the reference configuration is

$$\underline{\xi} = \mathbf{x}' - \mathbf{x} \quad (4.3)$$

The relative displacement of two material points is defined

$$\underline{\eta} = \mathbf{u}' - \mathbf{u}, \quad \mathbf{u} = \mathbf{y} - \mathbf{x} \quad (4.4)$$

where $\mathbf{y} = \chi(\mathbf{x}, t)$, is the mapping from the reference to the deformed configuration.

The deformation vector state field is defined as

$$\underline{\mathbf{Y}}[\mathbf{x}, t](\underline{\xi}) = \mathbf{y}' - \mathbf{y} = \mathbf{y}(\mathbf{x}', t) - \mathbf{y}(\mathbf{x}, t) = \mathbf{y}(\mathbf{x} + \underline{\xi}, t) - \mathbf{y}(\mathbf{x}, t). \quad (4.5)$$

See Figure 4-1 for clarification. An influence function, $w(\underline{\xi})$, which is required to be nonnegative on \mathcal{D} and satisfies $\int_{\mathcal{D}} w(\underline{\xi}) dV > 0$ is introduced. Typically we assume if $|\underline{\xi}| > \delta \rightarrow w(\underline{\xi}) = 0$, where δ is called the peridynamic horizon.

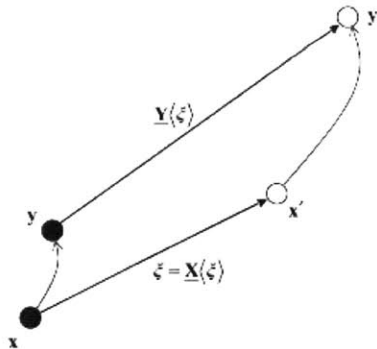


Figure 4-1: Deformation vector state (reproduced from [2])

4.2.2 Equations of motion

The governing equations of motion for a peridynamic body are given by:

$$\rho(\mathbf{x})\ddot{\mathbf{u}}(\mathbf{x}, t) = \int_{\mathcal{D}} \{\underline{\mathbf{T}}[\mathbf{x}, t]\langle \mathbf{x}' - \mathbf{x} \rangle - \underline{\mathbf{T}}[\mathbf{x}', t]\langle \mathbf{x} - \mathbf{x}' \rangle\} dV_{\mathbf{x}'} + \mathbf{b}(\mathbf{x}, t) \quad (4.6)$$

It has been shown [2] that for any bounded peridynamic body, \mathcal{B} , subjected to a body force density field \mathbf{b} , the equations satisfy balance of linear momentum. Consider the equations of motion integrated over an arbitrary peridynamic body:

$$\int_{\mathcal{B}} (\rho\ddot{\mathbf{u}} - \mathbf{b}) dV_{\mathbf{x}} = \int_{\mathcal{B}} \int_{\mathcal{B}} \{\underline{\mathbf{T}}[\mathbf{x}, t]\langle \mathbf{x}' - \mathbf{x} \rangle - \underline{\mathbf{T}}[\mathbf{x}', t]\langle \mathbf{x} - \mathbf{x}' \rangle\} dV_{\mathbf{x}'} dV_{\mathbf{x}}. \quad (4.7)$$

By considering the right term on the right hand side and switching dummy integration variables and reversing the order of integration we get:

$$\int_{\mathcal{B}} (\rho\ddot{\mathbf{u}} - \mathbf{b}) dV_{\mathbf{x}} = \int_{\mathcal{B}} \int_{\mathcal{B}} \{\underline{\mathbf{T}}[\mathbf{x}, t]\langle \mathbf{x}' - \mathbf{x} \rangle - \underline{\mathbf{T}}[\mathbf{x}', t]\langle \mathbf{x} - \mathbf{x}' \rangle\} dV_{\mathbf{x}'} dV_{\mathbf{x}} = 0 \quad (4.8)$$

which demonstrates that linear momentum is conserved as external forces are balanced by accelerations.

4.2.3 Constitutive correspondence

A major limitation was overcome with the development of state-based peridynamics. Combined with the idea of constitutive correspondence, the formulation is able to model any classical continuum constitutive law. Consider for now an elastic body. The idea of constitutive correspondence is simply to match the strain energy density computed from a traditional continuum constitutive law with that computed by the peridynamic state-based constitutive law under condition where the two are expected to be equivalent. Specifically, we will define first order correspondence as ensuring that any (locally) affine deformation of a peridynamic body will have the exact same elastic energy density as its corresponding classical body. One fairly straightforward

way to achieve this was detailed by Silling, *et al.* [2] as follows: compute

$$\mathbf{K} = \int_{\mathcal{D}} w(\boldsymbol{\xi}) \boldsymbol{\xi} \otimes \boldsymbol{\xi} d\boldsymbol{\xi}, \quad \bar{\mathbf{F}} = \int_{\mathcal{D}} w(\boldsymbol{\xi}) \underline{\mathbf{Y}}(\boldsymbol{\xi}) \otimes \boldsymbol{\xi} d\boldsymbol{\xi} \mathbf{K}^{-1}, \quad (4.9)$$

where $\mathbf{K}, \bar{\mathbf{F}} \in \mathbb{R}^{3 \times 3}$. This field tensor, \mathbf{K} , acts something like a shape function for computing approximate deformation gradients, and the deformation gradient like field tensor, $\bar{\mathbf{F}}$ will be identical to the traditional deformation gradient when the body is subjected to affine deformations. As proof, suppose the deformation is such that the deformation gradient \mathbf{F} is constant throughout the body:

$$\underline{\mathbf{Y}}(\boldsymbol{\xi}) = \mathbf{F} \boldsymbol{\xi} \quad (4.10)$$

then $\bar{\mathbf{F}} = \mathbf{F}$ as

$$\bar{\mathbf{F}} = \int_{\mathcal{D}} w(\boldsymbol{\xi}) \underline{\mathbf{Y}}(\boldsymbol{\xi}) \otimes \boldsymbol{\xi} d\boldsymbol{\xi} \mathbf{K}^{-1} \quad (4.11)$$

$$= \int_{\mathcal{D}} w(\boldsymbol{\xi}) \mathbf{F} \boldsymbol{\xi} \otimes \boldsymbol{\xi} d\boldsymbol{\xi} \mathbf{K}^{-1} \quad (4.12)$$

$$= \mathbf{F} \int_{\mathcal{D}} w(\boldsymbol{\xi}) \boldsymbol{\xi} \otimes \boldsymbol{\xi} d\boldsymbol{\xi} \mathbf{K}^{-1} \quad (4.13)$$

$$= \mathbf{F} \mathbf{K} \mathbf{K}^{-1} \quad (4.14)$$

$$= \mathbf{F}. \quad (4.15)$$

For an elastic peridynamic material, we compute the peridynamic force state as

$$\underline{\mathbf{T}} = \Delta W(\underline{\mathbf{Y}}) \quad (4.16)$$

where ΔW is the Frechet derivate of the strain energy density W with respect to the deformation vector state $\underline{\mathbf{Y}}$.

Using peridynamic correspondence, we can compute the strain energy density as $W(\bar{\mathbf{F}})$. Such a material will have exactly the same strain energy as its equivalent classical material if the deformation gradient is constant within the horizon radius δ .

We now compute the peridynamic force state as

$$\underline{\mathbf{T}} = \frac{\partial W}{\partial \bar{\mathbf{F}}} \Delta \bar{\mathbf{F}}(\underline{\mathbf{Y}}) \quad \rightarrow \quad \underline{\mathbf{T}}(\underline{\boldsymbol{\xi}}) = w(\underline{\boldsymbol{\xi}}) \mathbf{P}(\bar{\mathbf{F}}) \mathbf{K}^{-1} \underline{\boldsymbol{\xi}}, \quad (4.17)$$

where $\mathbf{P}(\bar{\mathbf{F}})$ is the Piola stress tensor evaluated from the constitutive law [2].

This method can also be used for any elastoplastic material, if we take W to be the elastic part of the strain energy density. It has been shown that the peridynamic equations of motion are guaranteed to conserve angular momentum if the Cauchy stress computed using peridynamic correspondence is symmetric [2]. This is true even if the weighting function $w(\underline{\boldsymbol{\xi}})$ is anisotropic. As peridynamic forces are computed by work conjugacy relations, an elastic peridynamic material always conserves energy.

4.3 Peridynamic discretization

The simplest and most straightforward approach to discretizing the peridynamic equations of motion is by approximating the integrals in the formulation but assuming that the peridynamic state is piecewise constant within the Voronoi volumes surrounding each node of the discretization. The discretization is made up of a collection of nodes which cover the body. The nodes are called particles from here on to distinguish them from finite element nodes, and as analogy with computational models of molecular dynamics with multi-body potential interactions. Intuitively, we expect this integration to be at least first order accurate, though we might expect the convergence will be second order accurate for special particle distributions. The notion of convergence in peridynamic discretization is slightly complicated by the addition of the horizon length scale, as both δ and the discretization size must be taken into account to determine the convergence to standard continuum mechanics [87].

To discretize state-based peridynamics with constitutive correspondence according to equations 4.9 and 4.17, two essential approximations must be made. The first is that the deformation gradient must be estimated by comparing displacements of neighboring nodes and discretizing the integrals in Equation 4.9. The second is that

the total strain energy must be approximated by integrating strain energy density, as given by the constitutive law, over the entire domain. Internal forces are then computed as the derivative of energy with respect to particle displacements.

For simplicity, consider an elastic material with elastic strain energy $W = \int_{\mathcal{D}} \psi(\mathbf{x}) dV$. We discretize \mathcal{D} with a cloud of points which carry both field variables and internal variables. Each point particle represents a region of the domain and has an associated volume and mass. With this discretization paradigm, the only variables are field variables such as displacements and velocities, and internal values at the N points in \mathcal{D} . We call the node locations in the reference configuration $\bar{\mathbf{x}}$, while the node locations in the deformed configuration are given by $\bar{\mathbf{y}}$. To approximate the total strain energy, the simplest way to evaluate the peridynamic integral is to sum contributions from each particle, weighted by their volume:

$$\bar{W} = \sum_N \bar{\psi}_N V_N, \quad (4.18)$$

where we approximate $\psi(\mathbf{x})$ as

$$\bar{\psi}(\bar{\mathbf{x}}) = \bar{\psi}(\bar{\mathbf{x}}, \bar{\mathbf{y}}(\bar{\mathbf{x}})) \quad (4.19)$$

All other integrals in the formulation are computed similarly, including the corresponding deformations gradient $\bar{\mathbf{F}}$, the internal forces, etc. The equations of motion are integrated in time using the Newmark time stepping algorithm, with Newmark parameters chosen for explicit time integration and second order accuracy [56], $\beta = 0$ and $\gamma = \frac{1}{2}$.

Applications using the peridynamics computational framework are presented in Chapter 5. Some of these applications required the implementation of a contact algorithm for preventing inter-penetration. As an initial attempt, we proceeded with the standard approach used in the peridynamic literature for contact [84]. The strategy is to apply pairwise penalty contact between particles, provided they are within a distance δ_c of each other. This penalty force is applied pairwise along the vector be-

tween the particles in the deformed configuration and is proportional to the depth of penetration, increasing as the particles approach each other linearly with spring constant, k . This method is consistent with the bond-based peridynamic theory and is the peridynamic version of penalty contact. Note that traction boundary conditions from classical continuum mechanics do not exist in peridynamics. Classical tractions must be transformed into body forces which act over a region near the boundary of the peridynamic body.

Chapter 5

Peridynamic Simulations of Impact

To test the capabilities of the new peridynamic theory for applications with severe deformations resulting from impact, we implemented discretization and time-integration routines for peridynamics using programming paradigms borrowed from the molecular dynamics community [93, 84] in C++. In particular, this requires having neighbor lists for each particle which update as the simulation progresses and as new particles begin to interact with each other. For peridynamics it is slightly more complicated, as two sets of neighbor lists are required. One list is needed for neighbors in the reference configuration, used to compute deformation gradients and strain energies, while another list is required for neighbors in the deformed configuration, used to compute contact forces (and potentially viscous forces, though this has yet to be explored). In this manner, one can view state-based peridynamics as a specific form of molecular dynamics, whose multi-body potential is designed to use traditional constitutive laws. This potential is derived such that the total strain energy of a body subjected to affine transformations (constant deformation gradient) computed by discretized peridynamics is identical to that computed by the corresponding finite element discretization. This insight also provides a straightforward approach to coupling peridynamic discretizations with finite elements. The peridynamic routines are linked to a materials library which has implementations of a variety of commonly used constitutive laws, such as Neo-Hookean extended to the compressible range, J2 plasticity, etc. Initial results indicate that this method has the potential to over-

come the well known challenges discussed in earlier chapters of simulating very large deformations and fracture.

5.1 Talyor impact test

Properties	Values
Density (kg/m^3)	8930
Young's Modulus (GPa)	117
Poisson's Ratio	0.35
Yield Stress (MPa)	400
Plastic Modulus (MPa)	100

Table 5.1: Material properties for copper used in Taylor impact simulations.

A standard benchmark test for validating a new numerical method for problems involving plastic deformation and high speed impact is the Taylor impact test [94, 4, 79]. This benchmark has already been used to validate peridynamic plasticity by comparison with experimental results using an unspecified constitutive law for aluminum [79]. Likewise, we use this test to validate our implementation of the method. The main difference between our implementation of peridynamic plasticity is in the peridynamic weighting function, $w(\boldsymbol{\xi})$. In previous implementations, this weighting function was taken to be constant withing the horizon, while we take it to be proportional to $\exp\left(\frac{-4.5\xi^2}{\delta^2}\right)$, where $\xi = |\boldsymbol{\xi}|$, so that closer particles have more influence on each other than particles which are further apart within the horizon. The factor 4.5 in the exponent was chosen to ensure that neighbors near a horizon radius, δ , apart have only limited influence on each other. The effect of this parameter on the simulation results has yet to be explored. We speculate that an appropriate choice of weighting function could match desired dispersion relations for long wavelength elastic waves, as this is possible analytically in specific cases for bond-based peridynamics [78, 77]. We also experiment with the dependence on the length scale by varying the horizon length from about 3 to 4 times the maximum length between adjacent particles.

The physical setup of the Taylor impact test has a solid copper cylinder impacting a rigid frictionless wall head-on at 227 meters per second. The material properties used to model copper with a J2 linear hardening plasticity law are shown in Table 5.1. The initial length of the bar is 32.4 mm and it has an initial diameter of 6.4 mm. Figure 5-1 shows the deformed final configuration of the bar after $80 \mu\text{s}$ as well as contours of the equivalent plastic strain. The computational model consists of 10,853 particles. At each particle location, both field and internal variables are stored. Table 5.1 lists the final length, final mushroom radius, and final maximum effective plastic strain as predicted by peridynamics using a variety of different peridynamic horizons. This same physical problem was recently analyzed in [4] using an alternative discretization and compared with existing computational results from the literature. These results are also included in Table 5.1 for comparison. The results indicate that the peridynamic solution matches well with the historical Taylor impact results for a variety of peridynamic horizon lengths, but experience shows that resolving the horizon is crucial to avoid numerical issues, and therefore the result using the largest horizon $\delta = 4.0L$, where L is characteristic length of the discretization, seems to produce the most accurate and stable solution.

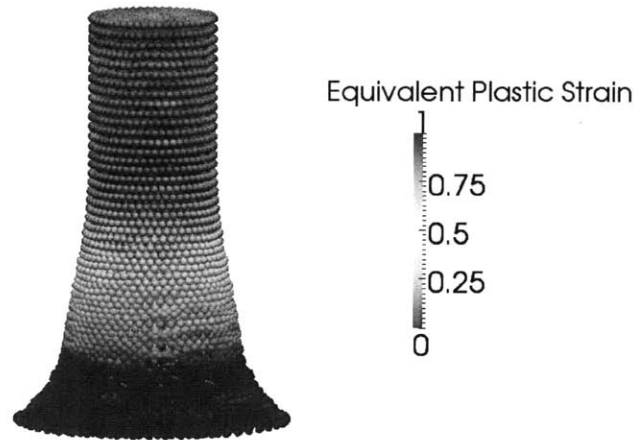


Figure 5-1: Deformed configuration of Taylor impact bar discretized using peridynamics

	Final length (mm)	Max. radius (mm)	Max. eff. plastic strain
Kamoulakis [95]	21.47-21.66	7.02-7.12	2.47-3.24
Zhu and Cescotto [96]	21.26-21.49	6.89-7.18	2.47-3.24
Camacho and Ortiz [55]	21.42-21.44	7.21-7.24	2.97-3.25
Li, Habbal and Ortiz [4]	21.43	6.8	3.0
Peridynamic, $\delta = 3.1L$	21.05	6.81	3.02
Peridynamic, $\delta = 3.6L$	21.1	6.87	2.92
Peridynamic, $\delta = 4.0L$	21.1	6.93	2.77

Table 5.2: Comparison of Taylor impact simulations (adapted from [4])

5.2 Ballistic impact on an aluminum sandwich structure

As a more complicated validation for the method, we simulated experiments described in [3]. The experiment we focus on consists of a hard steel spherical projectile impacting an aluminum sandwich panel structure with triangular shaped corrugation. A schematic of this structure is depicted in Figure 5-2. The performance and design of such sandwich structures subjected to impulsive loadings has recently received significant attention [97, 98, 99], focusing on, among other things, the properties of the materials, the structure topology and the strength of the joints.

We modeled the aluminum structure using the modified Johnson-Cook constitutive model with damage described in Chapter 2. The failure criterion considers the damage at a particle's material point location, and when it exceeds 0.99, all of its peridynamic bonds are cut. Contact is still allowed to occur among all particles, broken or unbroken. This is perhaps the simplest way to implement a damage law into peridynamics and is analogous to element deletion or material point deletion strategies in finite elements, with the benefit that broken particles can still interact mechanically with the system. An unfortunate consequence of this simplified failure criterion is that a failed region is certain to be broken into segments whose size is exactly the discretization size, as all bond's for a particle are broken at once. This results in the many broken particles observed in the simulation results instead of larger fragments with clusters of particles. The boundary conditions for the numerical setup matched

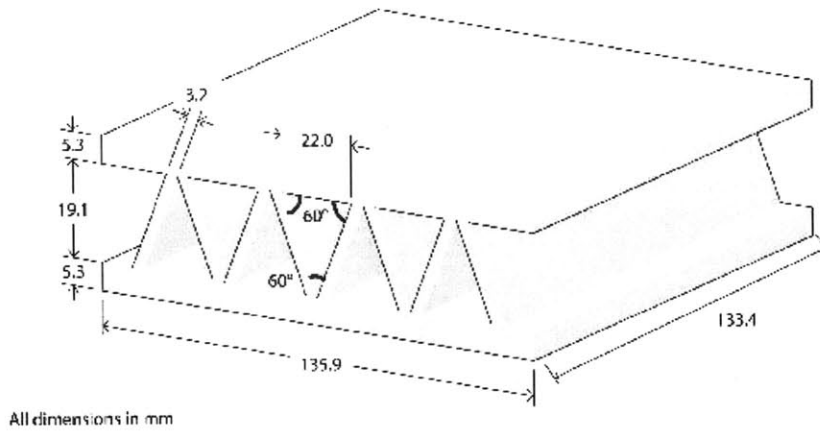


Figure 5-2: Schematic of sandwich panel (reproduced from [3])

the experiments by having the longitudinal edges completely confined. The 0.5055 inch diameter spherical steel projectile was modeled as an elastic solid using a finite element mesh, with density 7800 kg/m^3 , Young's modulus 200 GPa, and Poisson's ratio 0.25, assuming for simplicity that the plastic deformation of the projectile does not significantly affect the response of the sandwich structure. Coupling between the finite element mesh (projectile) and the peridynamic domain (sandwich structure) is accomplished in a straightforward manner by simply applying penalty contact forces between the nodes and particles whenever they passed within some pre-specified distance of one another. This form of contact is similar to what has been used in the peridynamic literature for particle-on-particle contact [84]. The peridynamic horizon radius was taken to be roughly three times the largest distance between neighboring particles, as experience has found this to be sufficiently large to ensure stability of the method.

Experiments and simulations were conducted using different initial impact velocities for the spherical projectile. Figure 5-3 shows example snapshots at various time steps for a simulation with an initial projectile velocity of 368 m/s. This velocity is

well below the ballistic limit, the impact velocity below which the projectile is defeated and above which it penetrates. In this case, the projectile penetrated the top face of the panels but is stopped by the corrugation. The appearance of so many “flying spheres” results partially from the fact that the simulation is under-resolved and partially from the nature of the failure criterion.

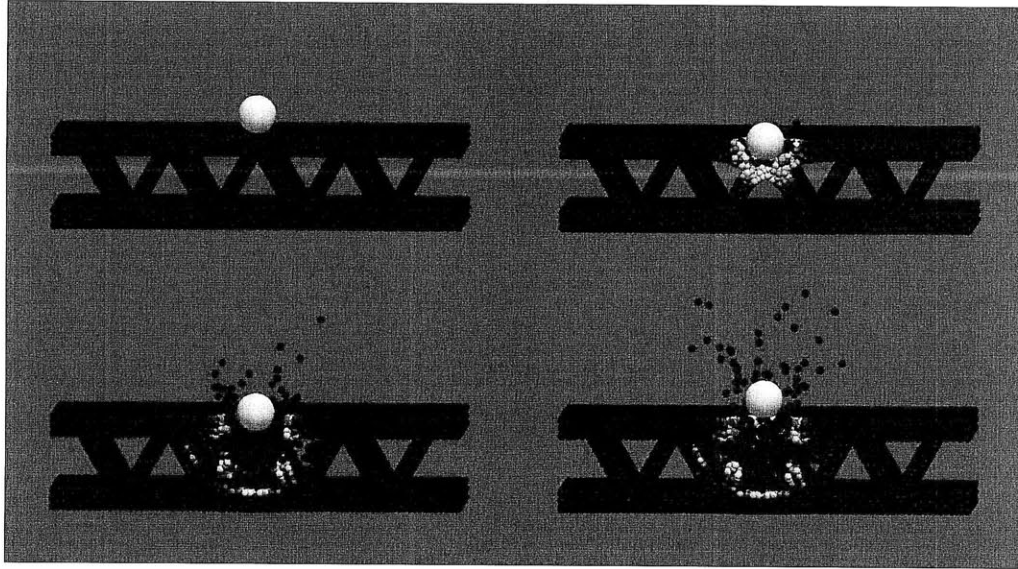


Figure 5-3: Snapshots of sandwich panel impacted at 368 m/s

Figure 5-4 shows example snapshots at various time-steps for a simulation with an initial projectile velocity of 531 m/s. This initial velocity is very close to the ballistic limit, as the projectile penetrates the top face and corrugation, but is *just* barely stopped by the back face.

Finally, Figure 5-5 shows example snapshots at various time steps for a simulation with an initial projectile velocity of 895 m/s. This velocity is much higher than the ballistic limit, so the projectile easily penetrated through the panel.

The numerically computed residual projectile velocity as a function of the initial impact velocity is shown in Figure 5-6 and is compared with the corresponding experimental results by Wetzell [3]. To obtain such accurate computational results it was necessary to tune the damage parameters in the modified Johnson-Cook constitutive law. We choose to consider the case where the initial projectile velocity was 740 m/s

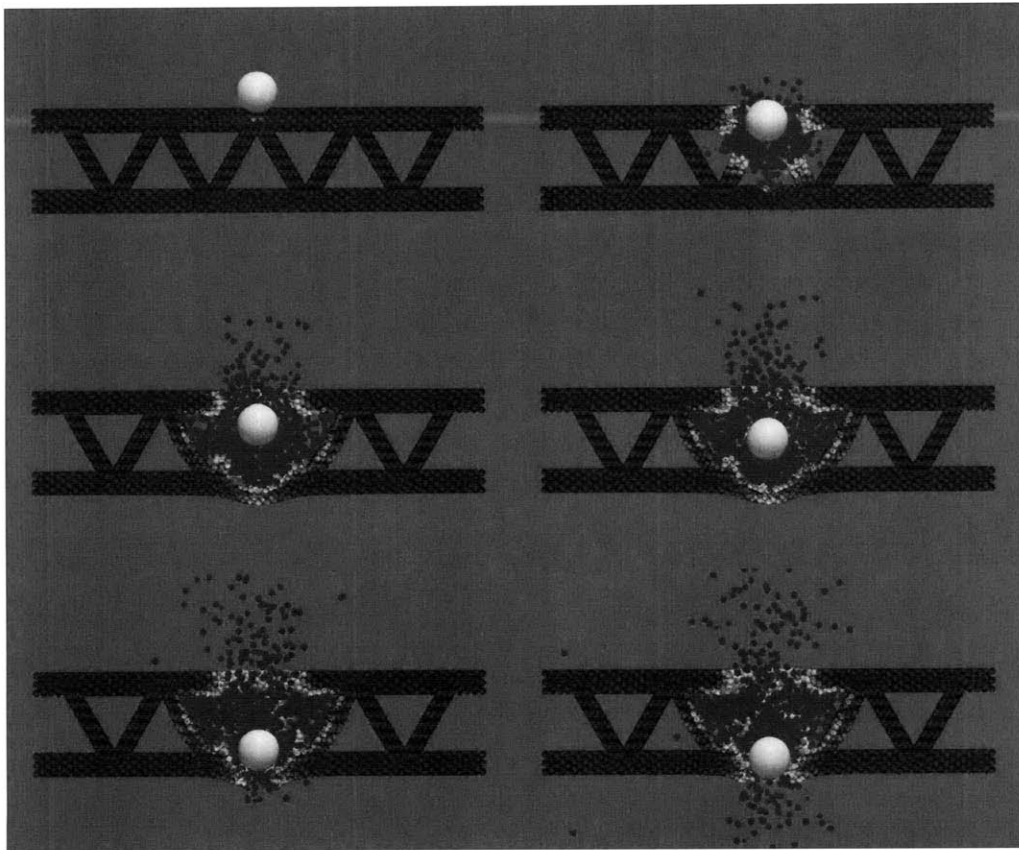


Figure 5-4: Snapshots of sandwich panel impacted at 531 m/s

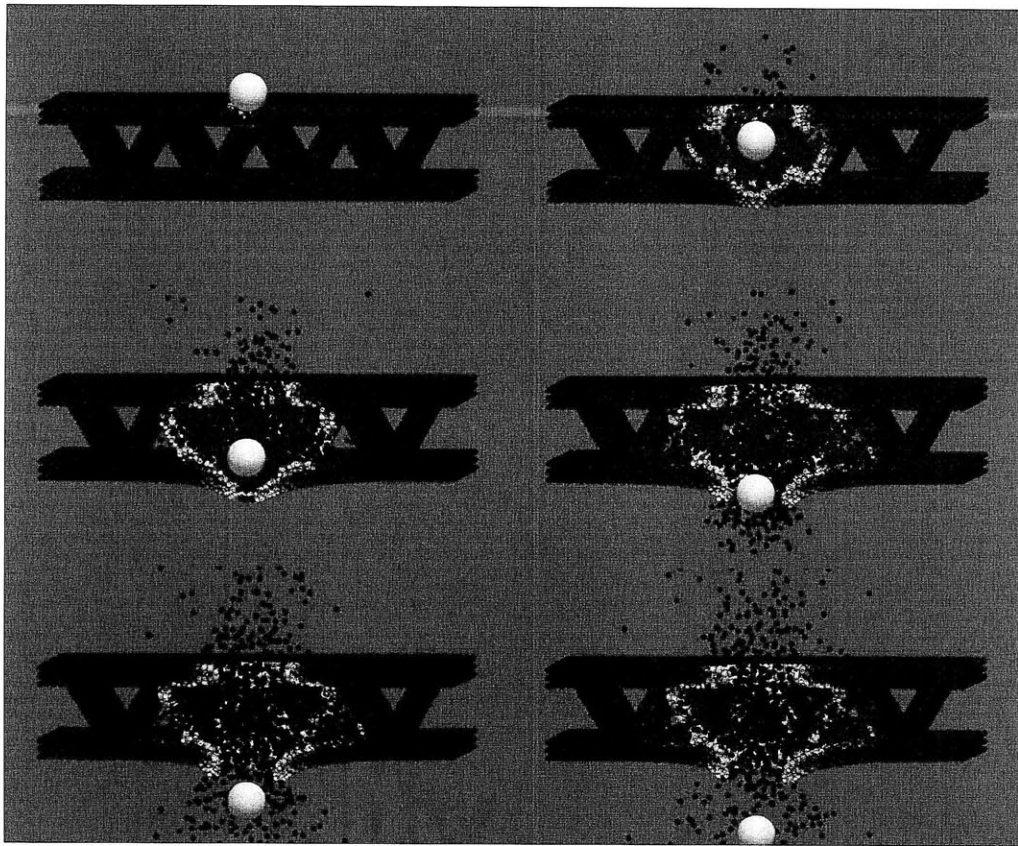


Figure 5-5: Snapshots of sandwich panel impacted at 895 m/s

and adjusted the fitting parameters of the damage evolution law to exactly reproduce the experimentally observed residual velocity for this case. All other residual velocities were predicted using those same parameters. Despite this necessary fitting, it is evident that the methodology shows much promise as a computational framework for ballistic impact simulations, with impressive capabilities especially considering the relative simplicity of its implementation.

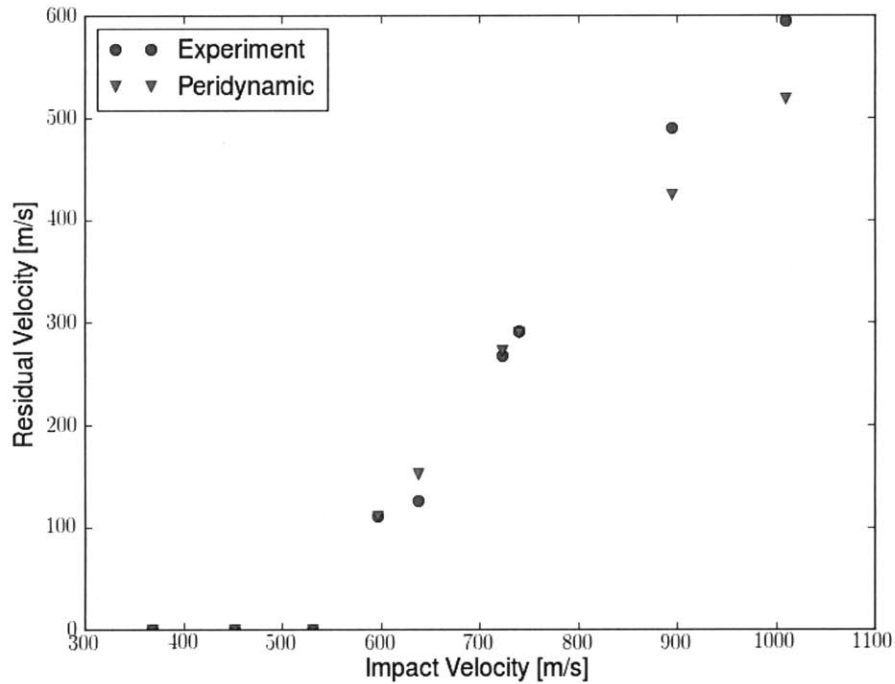


Figure 5-6: Numerical and experimental residual velocity vs. initial impact velocity for sandwich panel impact [3]

5.3 Crush test of an aluminum sandwich structure

As another test of the method which is not critically dependent on the damage law, we performed a quasi-static crush simulation. In the thesis by Wetzel [3], a quasi-static crush test was performed to determine the force displacement curve for the structure. Images from these experiments, reproduced from [3], are shown in Figure 5-7. The

experiment used the same structure as was used in the ballistic test in Section 5.2. Snapshots at a few time steps during the quasi-static crush test simulation are shown in Figure 5-8. The simulation results depict interesting bifurcations in the buckling modes of the triangular corrugation which are quite similar to the experiments. One of the structural member evens manages to flip its buckling direction half way along its length.

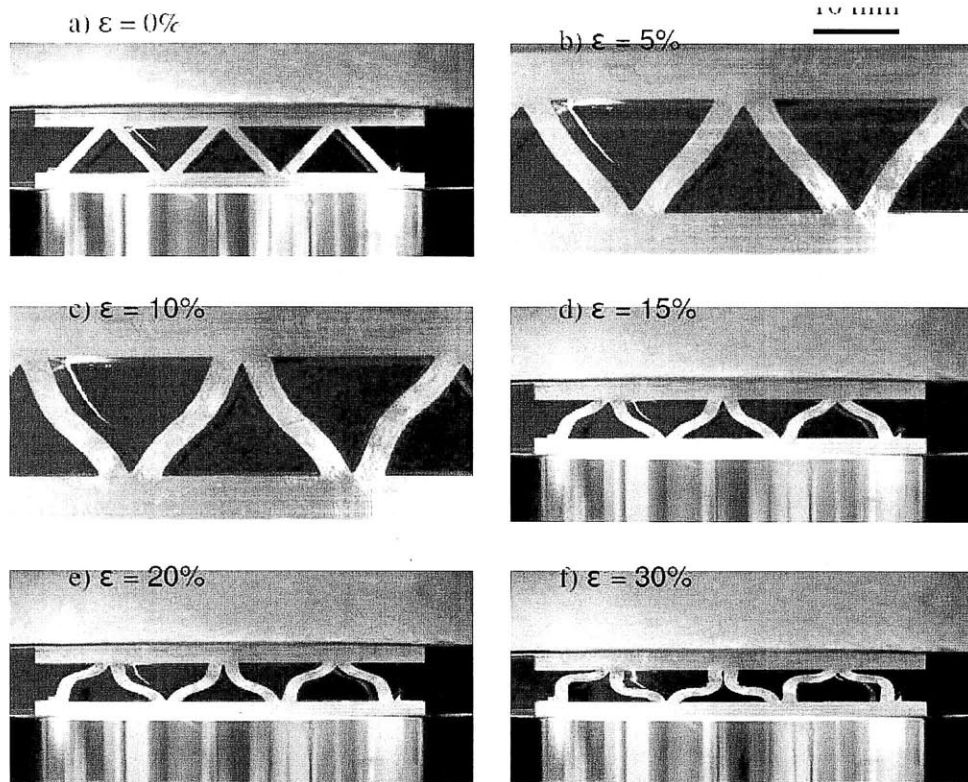


Figure 5-7: Quasi-static crush test of sandwich panels (reproduced from [3])

The computationally predicted force vs. displacement curve for two different refinement levels of the discretization are shown in Figure 5-9, together with the experimental results [3]. It is clear that the elastic portion of the curve is accurately reproduced, as are the magnitudes of the stress and critical strains. The refined mesh is even able to capture qualitatively the long softening regime when the plates are buckling, followed by a hardening regime where self contact between the structural elements begins to occur. The coarser discretization is unable to accurately capture

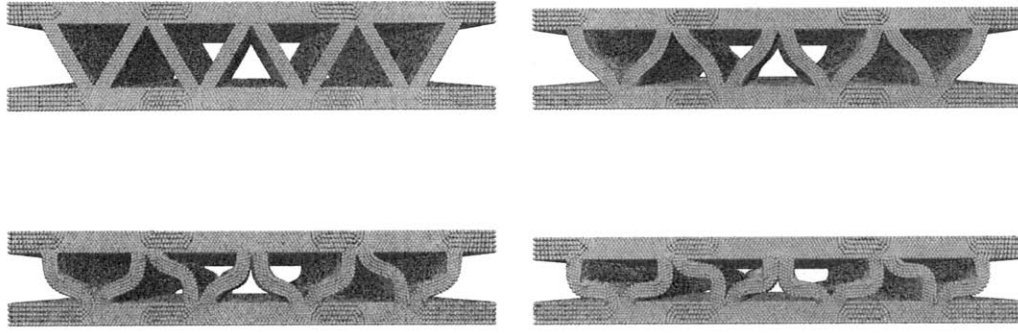


Figure 5-8: Quasi-static crushed sandwich panel discretized using peridynamics

this phenomenon as the peridynamic horizon is much larger, leading to earlier self contact and over stiffening due to the long distance interactions around the joints of the sandwich panels.

Peridynamics remains a relatively unexplored field and there still many potential opportunities for discovering and exploiting its advantages over traditional approaches. Some exciting avenues of research beyond the scope of this thesis are: exploring the fracture capturing capabilities based on novel non-local peridynamic inspired fracture criterion, improved numerical accuracy and parallelization, and integration within a more general computation framework.

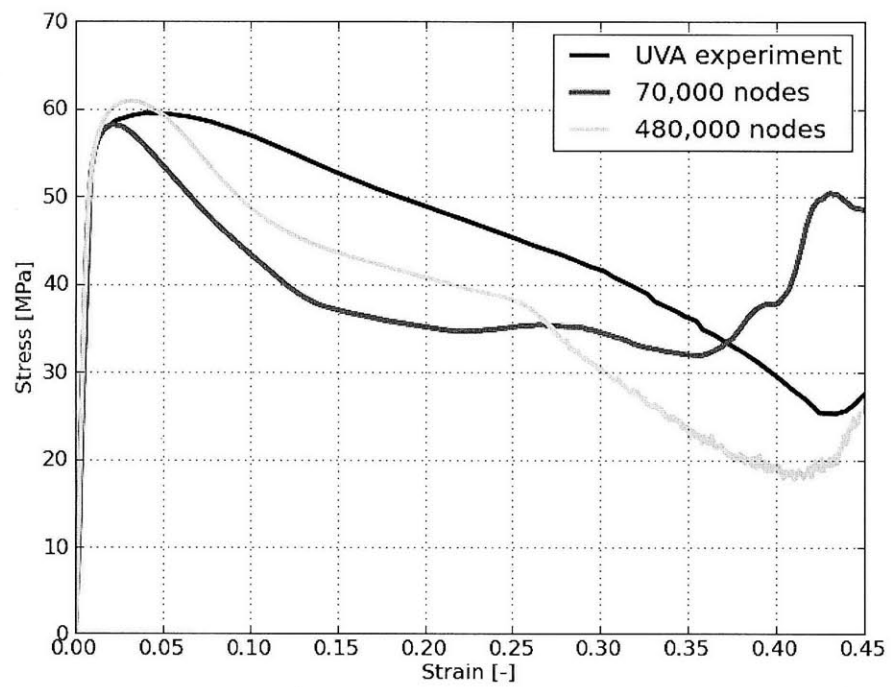


Figure 5-9: Force vs. displacement curve for crushed sandwich panels

Chapter 6

Summary and Conclusions

In this thesis, competing computational methods for simulating ballistic impact were investigated. An overview was provided of existing strategies using Lagrangian finite elements, meshless methods and particle methods, as well as Eulerian discretizations. For our initial investigation, we considered the traditional continuum mechanics formulation, discretized using the finite element method. Numerical examples were presented using the Deshpande-Evans ceramic damage model [46]. These results demonstrated the model's ability to predict experimentally observed crack patterns. Two extensions to the standard explicit dynamic finite element approach were required. First, an artificial viscosity component was added to the constitutive law to assist numerical stability in the presence of shocks. Second, a rigid body contact algorithm was developed, inspired by the decomposition contact response algorithm of Cirak and West [62]. Additional examples, which utilized adaptive remeshing algorithms, probed the limitations of the Lagrangian finite element method's ability to predict long rod penetration in a ceramic target and the transition from dwell to penetration. The full potential for this approach to modeling hypervelocity ballistic impact remains unclear, as even frequent adaptive remeshing was unable to avoid element inversion.

An alternative Lagrangian approach for predicting unconstrained plastic flow was then investigated, based on a discretization of the peridynamic formulation of continuum mechanics [34, 2]. The method permits the use of established continuum

constitutive laws within a particle-based computational framework. This approach was motivated by the limited success of finite element methods, which require a mesh, adaptive remeshing and field transfers for this class of impact problems. A validating benchmark example using the Taylor impact test was shown and compared with previous results from the literature. More complicated simulation setups involved ballistic impact of a spherical projectile on an aluminum sandwich structure and a crush test. These provided further demonstration of the methods ability and robustness in simulating complex material deformations. Preliminary results indicate that the peridynamic approach provides a convenient and straight forward framework from which to derive and implement continuum discretizations.

The results of this thesis suggest a variety of potential avenues for further research. The main conclusion from the finite element simulations is that adaptive remeshing strategies in their current form are unable to reliably maintain mesh quality during simulations of ballistic impact events. Initial results using Peridynamic discretizations, by contrast, indicate that the approach may have the ability to overcome several of the limitations of mesh based Lagrangian formulations. It must be cautioned that the peridynamic approach is still in its early stages of development and several unresolved issues remain to be addressed. Perhaps the most critical issue for any numerical discretization is its accuracy and order of convergence. Empirical evidence suggests that Peridynamic discretizations are first order accurate at best, though convergence rates and error estimates have yet to be analytically derived. We speculate that higher order versions of the theory are possible. A related issue is wave propagation and the complicated dispersion relations which the theory introduces. Further research into both the analytical and discretized dispersion relations of peridynamics could shed light on wave propagation issues for other particle based methods. Possibilities for further research also exist in specific application areas. For example, developing peridynamics as a tool for multi-scale physics problems requires advances in the coupling of peridynamics with other continuum discretizations, such as finite elements, as well as with molecular dynamics codes. Large scale simulations of metallic armor systems, on the other hand, require developments in modeling duc-

tile fracture within the peridynamics framework and would be significantly aided by parallel implementations.

Appendix A

Deshpande-Evans Damage Model

The strain energy density of the ceramic is assumed to depend on the triaxiality at a material point. Triaxiality Regime I models the crack response under highly compressive triaxiality. In this case, it is assumed that the compressive stresses are sufficient to close the wing-cracks and prevent sliding. This results in a strain energy density for the material equal to that of an uncracked ceramic:

$$W = W_0 = \frac{1}{4G} \left[\frac{2}{3} \bar{\sigma}^2 + \frac{3(1-2\nu)}{1+\nu} \sigma_m^2 \right] \quad (\text{A.1})$$

where ν is Poisson's ratio, G is the shear modulus, $\sigma_m = \frac{1}{3} \text{tr}(\boldsymbol{\sigma})$ is the mean stress and $\bar{\sigma} = \sqrt{\frac{3}{2} \boldsymbol{\sigma}' : \boldsymbol{\sigma}'}$ is the von Mises stress.

As the triaxiality become less negative, the model enters regime II, where it is assumed that the cracks are still closed, but that frictional sliding is allowed. This leads to a stress intensity factor at the crack tips of the form:

$$\frac{K_I}{\sqrt{\pi a}} = A \sigma_m + B \bar{\sigma} \quad (\text{A.2})$$

where A and B depend nonlinearly on the damage variable, D and the Coulomb friction coefficient, μ . The specific form for the parameters A and B in regime II are given by

$$A = c_1 (c_2 A_3 - c_2 A_1 + c_3) \quad (\text{A.3})$$

and

$$B = \frac{c_1}{\sqrt{3}} (c_2 A_3 + c_2 A_1 + c_3) \quad (\text{A.4})$$

where c_1 , c_2 , and c_3 are given by

$$c_1 = \frac{1}{\pi^2 \alpha^{3/2} \left[\left(\frac{D}{D_0} \right)^{1/3} - 1 + \frac{\beta}{\alpha} \right]^{3/2}}, \quad (\text{A.5})$$

$$c_2 = 1 + 2 \left[\left(\frac{D}{D_0} \right)^{1/3} - 1 \right]^2 \left(\frac{D_0^{2/3}}{1 - D^{2/3}} \right), \quad (\text{A.6})$$

and

$$c_3 = 2\alpha^2 \pi^2 \left[\left(\frac{D}{D_0} \right)^{1/3} - 1 \right]^2, \quad (\text{A.7})$$

and A_1 and A_3 are given by

$$A_1 = \pi \sqrt{\frac{\beta}{3}} \left[(1 + \mu^2)^{1/2} - \mu \right], \quad (\text{A.8})$$

$$A_3 = A_1 \left[\frac{(1 + \mu^2)^{1/2} + \mu}{(1 + \mu^2)^{1/2} - \mu} \right] \quad (\text{A.9})$$

and $\beta = 0.1$. The strain energy density function in Regime II is expressed as

$$W = W_0 + \frac{\pi D_0}{4\alpha^3 G (1 + \nu)} (A\sigma_m + B\bar{\sigma})^2. \quad (\text{A.10})$$

The transition between Regime I and Regime II occurs when K_I in Regime II approaches zeros at a triaxiality of

$$\lambda_{I \rightarrow II} = -\frac{B}{A}. \quad (\text{A.11})$$

As the triaxiality become even less compressive, the crack faces are allows to open. In this regime III, the stress intensity is given by the classical expression for a cracked elastic solid containing an isotropic distribution of wing-cracks [100, 101],

$$\frac{K_I}{\sqrt{\pi a}} = (C^2 \sigma_m^2 + E^2 \bar{\sigma}^2)^{1/2} \quad (\text{A.12})$$

where the parameters C and E are specified by matching the transition from Regime II to Regime III as

$$C = A + \gamma \sqrt{\alpha \left(\frac{D}{D_0} \right)^{1/3}} \quad (\text{A.13})$$

and

$$E^2 = \frac{B^2 C^2}{C^2 - A^2} \quad (\text{A.14})$$

with $\gamma = 2.0$.

In Regime III, the strain energy density is

$$W = W_0 + \frac{\pi D_0}{4\alpha^3 G (1 + \nu)} (C^2 \sigma_m^2 + E^2 \bar{\sigma}^2) \quad (\text{A.15})$$

The transition between regimes II and III occurs at a stress triaxiality give by

$$\lambda_{II \rightarrow III} = \frac{AB}{C^2 - A^2} \quad (\text{A.16})$$

as obtained in [46] by the proper transitioning between regimes II and III.

The evolution law for the crack length l is given by

$$\dot{l}/\dot{l}_0 = (K_I/K_{IC})^m \quad (\text{A.17})$$

where K_{IC} is the Mode I fracture toughness, m the rate sensitivity exponent, and \dot{l}_0 the reference crack growth rate at $K_I = K_{IC}$. Adding a restriction that the crack length is not allowed to propagate faster than the shear wave speed, the final crack-growth law is expressed

$$\dot{l} = \min \left[\dot{l}_0 \left(\frac{K_I}{K_{IC}} \right)^m, \sqrt{\frac{G}{\rho_0}} \right] \quad (\text{A.18})$$

where ρ_0 is the uncracked ceramic density.

Bibliography

- [1] P. Lundberg and B. Lundberg. Transition between interface defeat and penetration for tungsten projectiles and four silicon carbide materials. *International Journal of Impact Engineering*, 31:781–792, 2005.
- [2] S.A. Silling, M. Epton, O. Weckner, J. Xu, and E. Askari. Peridynamic states and constitutive modeling. *Journal of Elasticity*, 88:151–184, 2007.
- [3] J.J. Wetzel. The impulse response of extruded corrugated core aluminum sandwich structures. Master’s thesis, University of Virginia, 2009.
- [4] B. Li, F. Habbal, and M. Ortiz. Optimal transportation meshfree approximation schemes for fluid and plastic flows. *International Journal for Numerical Methods in Engineering*, 2010.
- [5] P. DiMarco. Navy foreign object damage and its impact on future gas turbine engine low pressure compression systems. *Propulsion and Energetics Panel Symposium: Erosion, Corrosion and Foreign Object Damage Effects in Gas Turbines*, 1994.
- [6] E.P. Fahrenthold and R. Shivarama. Orbital debris impact simulation using a parallel hybrid particle-element code. *International Journal of Impact Engineering*, 26:179–188, 2001.
- [7] T. Kenkmann, F. Horz, and A. Deutsch, editor. *Large meteorite impacts III*. The Geological Society of America, Boulder, Colorado, 2005.
- [8] A. Seagraves and R. Radovitzky. *Dynamic Failure of Materials and Structures*, chapter 12 Advances in Cohesive Zone Modeling of Dynamic Fracture, pages 349–405. Springer, 2009.
- [9] G.C. Bessette, E.B. Becker, L.M. Taylor, and D.L. Littlefield. Modeling of impact problems using an h-adaptive, explicit lagrangian finite element method in three dimensions. *Computer Methods in Applied Mechanics and Engineering*, 192:1649–1679, 2003.
- [10] G.T. Camacho and M. Ortiz. Computational modeling of impact damage in brittle materials. *International Journal of Solids and Structures*, 33(20–22):2899–2983, 1996.

- [11] D.J. Benson. Computational methods in lagrangian and eulerian hydrocodes. *Computer Methods in Applied Mechanics and Engineering*, 99:235–394, 1992.
- [12] J.M. McGlaun and S.L. Thompson. CTH: a three-dimensional shock wave physics code. *International Journal of Impact Engineering*, 10:351–360, 1990.
- [13] L.B. Lucy. A numerical approach to the testing of the fission hypothesis. *The Astronomical Journal*, 82:1013–1024, 1977.
- [14] R.A. Gingold and J.J. Monaghan. Smoothed particle hydrodynamics: theory and application to non-spherical stars. *Monthly Notices of the Royal Astronomical Society*, 181:375–389, 1977.
- [15] J.J. Monaghan. An introduction to SPH. *Computer Physics Communications*, 48:89–96, 1988.
- [16] J.J. Monaghan. Smoothed particle hydrodynamics. *Reports on Progress in Physics*, 68:1703–1759, 2005.
- [17] W.G. Hoover. Smooth-particle applied mechanics: Conservation of angular momentum with tensile stability and velocity averaging. *Physical Review E*, 69, 2004.
- [18] R.F. Stellingwerf and C.A. Wingate. Impact modeling with smooth particle hydrodynamics. *Società Astronomica Italiana*, 65:1117–1128, 1994.
- [19] G.R. Johnson, R.A. Stryk, and S.R. Beissel. SPH for high velocity impact computations. *Computer Methods in Applied Mechanics and Engineering*, 139:347–373, 1996.
- [20] C.E. Zhou, G.R. Liu, and X. Han. Classic taylor-bar impact test revisited using 3D SPH. *G.R. Liu et al. (eds.), Computational Methods*, pages 1405–1409, 2010.
- [21] G.R. Johnson and R.A. Stryk. Conversion of 3D distorted elements into meshless particles during dynamic deformation. *International Journal of Impact Engineering*, 28(9):947 – 966, 2003.
- [22] B. Nayroles, G. Touzot, and P. Villon. Generalizing the finite element method: diffuse approximation and diffuse elements. *Computational Mechanics.*, 10:307–318, 1992.
- [23] T. Belytschko, Y.Y. Lu, and L. Gu. Element-free Galerkin methods. *International Journal for Numerical Methods in Engineering*, 37:229–256, 1994.
- [24] W.K. Liu, S. Jun, and Y.F. Zhang. Reproducing kernel particle methods. *International Journal for Numerical Methods in Fluids*, 20:1081–1106, 1995.
- [25] W.K. Liu, S. Li, and T. Belytschko. Moving least square reproducing kernel methods (I) methodology and convergence. *Computer Methods in Applied Mechanical Engineering*, 143:113–154, 1997.

- [26] C.A.M. Duarte and J.T. Oden. H-p clouds an h-p meshless method. *Numerical Methods for Partial Differential Equations*, 12:673–705, 1996.
- [27] J.M. Melenk and I. Babuska. The partition of unity finite element method: basic theory and applications. *Computer Methods in Applied Mechanical Engineering*, 139:280–314, 1996.
- [28] S.N. Atluri and T. Zhu. A new Meshless Local Petrov-Galerkin (MLPG) approach in computational mechanics. *Computational Mechanics*, 22:117–127, 1998.
- [29] S. De and J. Bathe. The method of finite spheres. *Computational Mechanics*, 25:329–345, 2000.
- [30] M. Arroyo and M. Ortiz. Local maximum-entropy approximation schemes: a seamless bridge between finite elements and meshfree methods. *International Journal for Numerical Methods in Engineering*, 65:2167–2202, 2006.
- [31] Z.D. Han, H.T. Liu, A.M. Rajendran, and S.N. Atluri. The applications of meshless local Petrov-Galerkin (MLPG) approaches in high-speed impact, penetration and perforation problems. *Computer Modeling in Engineering & Sciences*, 14:119–128, 2006.
- [32] Y.Y. Zhang and L. Chen. Impact simulation using simplified meshless method. *International Journal of Impact Engineering*, 36:651–658, 2009.
- [33] E.P. Fahrenthold and B.A. Horban. A hybrid particle-finite element method for hypervelocity impact simulation. *International Journal of Impact Engineering*, 23:237–248, 1999.
- [34] S.A. Silling. Reformulation of elasticity theory for discontinuities and long-range forces. *Journal of the Mechanics and Physics of Solids*, 48:175–209, 2000.
- [35] G.R. Johnson and W.H. Cook. A constitutive model and data for metals subjected to large strains, high strain rates and high temperatures. In *Proceedings of the 7th International Symposium on Ballistics*, pages 541–547, The Hague, Netherlands, 1983.
- [36] G.R. Johnson and W.H. Cook. Fracture characteristics of three metals subjected to various strains, strain rates, temperatures and pressures. *Engineering Fracture Mechanics*, 21:31–48, 1985.
- [37] V.S. Deshpande, R.M. McMeeking, H.N.G. Wadley, and A.G. Evans. Constitutive model for predicting dynamic interactions between soil ejecta and structural panels. *Journal of the Mechanics and Physics of Solids*, 57:1139–1164, 2009.
- [38] A. Lew, R. Radovitzky, and M. Ortiz. An artificial-viscosity method for the lagrangian analysis of shocks in solids with strength on unstructured, arbitrary-order tetrahedral meshes. *Journal of Computer-Aided Materials Design*, 8(2-3):213–231, 2001.

- [39] Z.P. Bazant and M. Jirasek. Nonlocal integral formulations of plasticity and damage: Survey of Progress. *Journal of Engineering Mechanics*, 128:1119–1149, 2002.
- [40] J.C. Simo and T.J.R. Hughes. *Computational Inelasticity*. Springer, Berlin, 1998.
- [41] L. Anand. Constitutive equations for the rate-dependent deformation of metals at elevated temperatures. *Journal of Engineering Materials and Technology*, 104:12–17, 1982.
- [42] R. Radovitzky and M. Ortiz. Error estimation and adaptive meshing in strongly nonlinear dynamic problems. *Computer Methods in Applied Mechanics and Engineering*, 172:203–240, 1999.
- [43] M. Ortiz and L. Stainier. The variational formulation of viscoplastic updates. *Computer Methods in Applied Mechanics and Engineering*, 171:419–444, 1999.
- [44] Q. Yang, L. Stainier, and M. Ortiz. A variational formulation of the coupled thermo-mechanical boundary-value problem for general dissipative solids. *Journal of the Mechanics and Physics of Solids*, 54:401–424, 2006.
- [45] A. Ockewitz and D. Sun. Damage modelling of automobile components of aluminium materials under crash loading. *LS-DYNA Anwenderforum*, 2006.
- [46] V.S. Deshpande and A.G. Evans. Inelastic deformation and energy dissipation in ceramics: a mechanism-based constitutive model. *Journal of the Mechanics and Physics of Solids*, 56:3077–3100, 2008.
- [47] P.D. Zavattieri and H.D. Espinosa. Grain level analysis of crack initiation and propagation in brittle materials. *Acta Materialia*, 49:4291–4311, 2001.
- [48] H.D. Espinosa and P.D. Zavattieri. A grain level model for the study of failure initiation and evolution in polycrystalline brittle materials. part i: Theory and numerical implementation. *Mechanics of Materials*, 35:333–364, 2003.
- [49] H.D. Espinosa and P.D. Zavattieri. A grain level model for the study of failure initiation and evolution in polycrystalline brittle materials. part ii: Numerical examples. *Mechanics of Materials*, 35:365–394, 2003.
- [50] S. Maiti and P.H. Geubelle. Mesoscale modeling of dynamic fracture of ceramic materials. *Computer Methods in Engineering Sciences*, 5(2):2618–2641, 2004.
- [51] S. Maiti, K. Rangaswamy, and P.H. Geubelle. Mesoscale analysis of dynamic fragmentation of ceramics under tension. *Acta Materialia*, 53:823–834, 2005.
- [52] D.H. Warner, F. Sansoz, and J.F. Molinari. Atomistic based continuum investigation of plastic deformation in nanocrystalline copper. *International Journal of Plasticity*, 22:754–774, 2006.

- [53] Z. Wei, V.S. Deshpande, and A.G. Evans. The influence of material properties and confinement on the dynamic penetration of alumina by hard spheres. *Journal of Applied Mechanics*, 76:1–8, 2009.
- [54] M.F. Ashby and C.G. Sammis. The damage mechanics of brittle solids in compression. *Pageoph*, 133:489–521, 1990.
- [55] G. T. Camacho and M. Ortiz. Adaptive lagrangian modelling of ballistic penetration of metallic targets. *Computer Methods in Applied Mechanics and Engineering*, 142:269–301, 1997.
- [56] T. Belytschko and T.J.R. Hughes. *Computational Methods for Transient Analysis*. Elsevier Science, North-Holland, 1983.
- [57] T.D. Marusich and M. Ortiz. Modeling and simulation of high-speed machining. *International Journal for Numerical Methods in Engineering*, 38(21):3675–3694, 1995.
- [58] S. Yadav, E.A. Repetto, G. Ravichandran, and M. Ortiz. A computational study of the influence of thermal softening on ballistic penetration in metals. *International Journal of Impact Engineering*, 25:787–803, 2001.
- [59] S. Mauch, L. Noels, Z. Zhao, and R. Radovitzky. Lagrangian simulation of penetration environments via mesh healing and adaptive optimization. In A. M. Rajendran, W. Bryzik, B. J. Walker, J. W. McCauley, J. Reifman, and N. M. Nasrabadi, editor, *25th US Army Science Conference*, Orlando, FL, November, 2006.
- [60] R. Radovitzky and M. Ortiz. Tetrahedral mesh generation based on node insertion in crystal lattice arrangements and advancing-front-delaunay triangulation. *Computer Methods in Applied Mechanics and Engineering*, 187:543–569, 2000.
- [61] M. Ortiz and J.J. Quigley. Adaptive mesh refinement in strain localization problems. *Computer Methods in Applied Mechanics and Engineering*, 90:781–804, 1991.
- [62] F. Cirak and M. West. Decomposition contact response (dcr) for explicit finite element dynamics. *International Journal for Numerical Methods in Engineering*, 64:1078–1110, 2005.
- [63] J.O. Hallquist, G.L. Goudreau, and D.J. Benson. Sliding interfaces with contact-impact in large-scale lagrangian computations. *Computer Methods in Applied Mechanics and Engineering*, 51:107–137, 1985.
- [64] N.J. Carpenter, R.L. Taylor, and M.G. Katona. Lagrange constraints for transient finite-element surface-contact. *International Journal for Numerical Methods in Engineering*, 32:103–128, 1991.

- [65] T. Belytschko, W.K. Liu, and B. Moran. *Nonlinear Finite Elements for Continua and Structures*. John Wiley & Sons, 2000.
- [66] T.A. Laursen. *Computational Contact and Impact Mechanics*. Springer Verlag, 2002.
- [67] A. Pandolfi, C. Kane, J.E. Marsden, and M. Ortiz. Time-discretized variational formulation of non-smooth frictional contact. *International Journal for Numerical Methods in Engineering*, 53:1801–1829, 2002.
- [68] T.J. Holmquist and G.R. Johnson. Response of silicon carbide to high velocity impact. *Journal of Applied Physics*, 91:5858–5866, 2002.
- [69] G.R. Johnson and T.J. Holmquist. A computational constitutive model for brittle materials subjected to large strains, high strain rates and high pressures. In *EXPLOMET Conference*, San Diego, CA, 1990.
- [70] P. Lundberg, R. Renstrom, and B. Lundberg. Impact of metallic projectiles on ceramic targets: transition between interface defeat and penetration. *International Journal of Impact Engineering*, 24:259–275, 2000.
- [71] A.P.T.M.J.. Lamberts. *Numerical simulation of ballistic impact on ceramic material*. PhD thesis, Eindhoven University of Technology, 2007.
- [72] G.R. Johnson, T.J. Holmquist, and S.R. Beissel. Response of aluminum nitride (including phase change) to large strains, high strain rates and high pressures. *Journal of Applied Physics*, 94:1639–1646, 2003.
- [73] Z. Fawaz, W. Zheng, and K. Behdinan. Numerical simulation of normal and oblique ballistic impact on ceramic composite armours. *Composite Structures*, 63:387–395, 2004.
- [74] F. Zok. Personal Communication, 2009.
- [75] Mindlin, R.D. Second gradient of strain and surface-tension in linear elasticity. *International Journal of Solids and Structures*, 1:417–438, 1965.
- [76] A.C. Eringen. Linear theory of nonlocal elasticity and dispersion of plane waves. *International Journal of Engineering Science*, 10:425–435, 1972.
- [77] O. Weckner, G. Brunk, M.A. Epton, S.A. Silling, and E. Askari. Green’s functions in non-local three-dimensional linear elasticity. *Proceedings of the Royal Society A*, 465:3463–3487, 2009.
- [78] O. Weckner and R. Abeyaratne. The effect of long-range forces on the dynamics of a bar. *Journal of the Mechanics and Physics of Solids*, 53:705–728, 2005.
- [79] J.T. Foster, S.A. Silling, and W.W. Chen. Viscoplasticity using peridynamics. *International Journal for Numerical Methods in Engineering*, 81:1242–1258, 2010.

- [80] M. Müller, R. Keiser, A. Nealen, M. Pauly, M. Gross, and M. Alexa. Point based animation of elastic, plastic and melting objects. *Eurographics Symposium on Computer Animation*, 2004.
- [81] S.A. Silling and F. Bobaru. Peridynamic modeling of membranes and fibers. *International Journal of Non-Linear Mechanics*, 40:395–409, 2004.
- [82] S.A. Silling and E. Askari. A meshfree method based on the peridynamic model of solid mechanics. *Computers and Structures*, 83:1526–1535, 2005.
- [83] E. Askari, F. Bobaru, R.B. Lehoucq, M.L. Parks, S.A. Silling, and O. Weckner. Peridynamics for multiscale materials modeling. *Journal of Physics: Conference Series*, 125, 2008.
- [84] M.L. Parks, R.B. Lehoucq, S. Plimpton, and S. Silling. Implementing peridynamics within a molecular dynamics code. *Computer Physics Communications*, 179:777–783, 2008.
- [85] S.A. Silling, O. Weckner, E. Askari, and F. Bobaru. Crack nucleation in a peridynamic solid. *International Journal of Fracture*, 162:219–227, 2010.
- [86] Y.D. Ha and F. Bobaru. Studies of dynamic crack propagation and crack branching with peridynamics. *International Journal of Fracture*, 162:229–244, 2010.
- [87] F. Bobaru and M. Duangpanya. The peridynamic formulation for transient heat conduction. *International Journal of Heat and Mass Transfer*, published online June 4, 2010.
- [88] K. Dayal and K. Bhattacharya. Kinetics of phase transformations in the peridynamic formulation of Continuum Mechanics. *Journal of the Mechanics and Physics of Solids*, 54:1811–1842, 2006.
- [89] R.W. Macek and S.A. Silling. Peridynamics via finite element analysis. *Finite Elements in Analysis and Design*, 43:1169–1178, 2007.
- [90] S.A. Silling, M. Zimmermann, and R. Abeyaratne. Deformation of a peridynamic bar. *Journal of Elasticity*, 73:173–190, 2003.
- [91] E. Emmrich and O. Weckner. On the well-posedness of the linear peridynamic model and its convergence towards the Navier equation of linear elasticity. *Communications in Mathematical Sciences*, 5:851–864, 2007.
- [92] S.A. Silling and R.B. Lehoucq. Convergence of peridynamics to classical elasticity theory. *Journal of Elasticity*, 93:13–37, 2008.
- [93] S.J. Plimpton. Fast parallel algorithms for short-range molecular dynamics. *Journal of Computational Physics*, 117:1–19, 1995.

- [94] F. Zhou, J.F. Molinari, and K.T. Ramesh. An elastic-visco-plastic analysis of ductile expanding ring. *International Journal of Impact Engineering*, 33:880–891, 2006.
- [95] A. Kamoulakos. A simple benchmark for impact. *Benchmark*, pages 31–35, 1990.
- [96] Y.Y. Zhu and S. Cescotto. Unified and mixed formulation of the 4-node quadrilateral elements by assumed strain method: application to thermomechanical problems. *International Journal for Numerical Methods in Engineering*, 38:685–716, 1995.
- [97] L.F. Mori, S. Lee, Z.Y. Xue, A. Vaziri, D.T. Queheillalt, K.P. Dharmasena, H.N.G. Wadley, J.W. Hutchinson, and H.D. Espinosa. Deformation and fracture modes of sandwich structures subjected to underwater impulsive loads. *Journal of Mechanics of Materials and Structures*, 2:1981–2006, 2007.
- [98] H.N.G. Wadley. Multifunctional periodic cellular metals. *Philosophical Transactions of the Royal Society A*, 364:31–68, 2006.
- [99] T. Rabczuk, E. Samaniego, and T. Belytschko. Simplified model for predicting impulse loads on submerged structures to account for fluid-structure interaction. *International Journal of Impact Engineering*, 34:163–177, 2007.
- [100] J.R. Bristow. Microcracks, and the static and dynamic elastic constants of annealed and heavily cold-worked metals. *British Journal of Applied Physics*, 11:81–85, 1960.
- [101] B. Budiansky and R.J. O’Connell. Elastic moduli of a cracked solid. *International Journal of Solids and Structures*, 12:81–97, 1976.